Advances in Water Resources 188 (2024) 104710

Contents lists available at ScienceDirect

Advances in Water Resources

journal homepage: www.elsevier.com/locate/advwatres

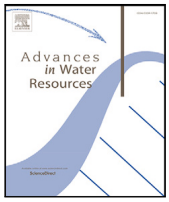

Mixing-phase model for shear-induced contractive/dilative effects in unsteady water-sediment mixture flows

S. Martínez-Aranda *, J. Fernández-Pato, P. García-Navarro

Fluid Dynamic Technologies – I3A, University of Zaragoza, Spain

ARTICLE INFO

Keywords:
Water-sediment shallow flows
Non-Newtonian rheology
Pore-fluid pressure
Contractive/dilative mixtures
Geophysical surface hazards

ABSTRACT

Among the geophysical surface processes, mud and debris flows show one of the most complex and challenging behaviour for scientists and modellers. These flows consist of highly-unsteady gravity-driven movements of water-sediment mixtures with non-Newtonian rheology where the solid concentration could be about 40%–80% of the flow volume and which occur along steep and irregular terrains. Furthermore, the appearance of dynamic pressures in the fluid filling the intergranular pores increases the complexity and dominates the behaviour of the fluidized water-sediment material, leading to the appearance of significant density gradients during the movement. The dynamic pressure in the pore-fluid changes the effective normal stress within the mobilized material, affecting the frictional shear stress between grains and leading to the solid phase dilation/contraction. This must be properly accounted for when developing realistic models for water-sediment surface flows. In this work, a novel physically-based approach for modelling multi-grain dense-packed water-sediment flows is presented. A novel closure formulation for the pressure distribution within the pore-fluid during the movement of dense-packed water-sediment materials has been derived. This closure allows to relate the appearance of shear-induced dynamic pore pressures to the contractive/dilative behaviour of the solid aggregate. The resultant system of depth-averaged conservation laws includes continuity of the density-variable water-sediment material and the different solid classes transported in the flow, as well as the linear momentum equation for the fluidized bulk material, and it is solved using a well-balanced fully-coupled Finite Volume (FV) method. The resultant simulation tool is faced to synthetic, laboratory and real-scale benchmark cases to test its robustness and accuracy. The presence of dynamic pore pressures within the pore-fluid leads to the appearance of a deviatoric contribution to the solid flux, which causes the shear-induced separation of the solid and liquid phases and sustains the flow mobility for long distances, as it has been observed in real mud and debris events.

1. Introduction

Landslides, debris aggregates, natural muds or mining tailings are considered highly solid-laden fluids in which the solid phase can represent almost 80% of the volume and hence the bulk density of the water-solid aggregate can be even twice or three times the water density (Iverson, 1997). The origin, shape and size of the transported solids might vary from large boulders and tree stumps to very fine materials, such as fine clay or heavy metal particles. In debris flows, coarse sediment fractions (sand, gravels and pebbles) predominate in the solid phase whereas fine fractions, such as silt and clay, are typical for mud flows. Furthermore, debris flows show plasticity index lower than 5% and, contrarily, muddy slurries are usually characterized by plasticity index larger than 5% (Hungr et al., 2001). The bulk water-sediment mixture in motion is denoted as fluidized material all over the text, regardless the nature, size and concentration of the solid phase.

The presence of the solid phase, especially the fine sediments as silt or clay, affects the rheological behaviour of the fluidized material. The fluid filling the pores is composed of water and fine solid particles. This intergranular fluid shows a critical yield strength which allows that coarse solid particles, such as gravels or even pebbles, can be suspended indefinitely in the flow column (Pierson, 2005; Calhoun and Clague, 2018). Apparently, this fine material mixed in the pore-fluid is responsible for the development and maintenance of an excess of pressure in the intergranular fluid during the triggering and motion of mud/debris flows, causing the actual liquefaction of the aggregate material (Rodine and Johnson, 1976; Jakob and Hungr, 2005). Furthermore, typically the front of the debris wave contains most of the coarse materials whereas the tail shows a more liquefied composition. Usually, mud and debris flows mobilize from landslides due to an excess of intergranular water, and this segregation of the material occurred during

* Corresponding author.
E-mail address: sermar@unizar.es (S. Martínez-Aranda).

https://doi.org/10.1016/j.advwatres.2024.104710
Received 24 September 2023; Received in revised form 2 April 2024; Accepted 19 April 2024
Available online 24 April 2024

the movement is mainly caused by the dilation of the solid aggregate. The transformation from solid to fluid behaviour is recognized in saturated, contractive granular soils due to liquefaction (Sassa, 1984). However, dominantly dilative transformation from solid landslide to fluid debris flow has been reported (Fleming et al., 1989). Therefore, the transformations from a contractive/dilative "solid like" material to a fully developed mud/debris flow is a complex process where multiple simultaneous phenomena occur but the persistence of pore-pressure excess seems to be responsible for the dilation and segregation of the coarser solid material, and for sustaining the movement of fluidized material for long distances (McArdell et al., 2007; Iverson et al., 2010).

The mathematical modelling of this kind of surface flows of water-sediment mixtures is a challenging topic due to the high uncertainty associated to the varying solid-fluid composition. In the last decade, an important effort has been paid to get insight into the physical behaviour of this kind of multi-phase continuum materials at small-scales, specially for the study of submerged granular currents and debris flows. Novel approaches have been proposed to model the complex 3D interaction and evolution of liquid and solid elements into the bulk material motion, including coupled Lattice-Boltzmann and Discrete Element methods for grain-scale interaction problems (Tsigginos et al., 2022; Ding and Xu, 2018), Material Point Method applied to laboratory-scale partially-saturated granular flows (Baumgarten and Kamrin, 2019; Vicari et al., 2022) and continuum two-phase modelling for the failure of submerged granular columns (Lee, 2021; Montellà et al., 2023). Special mention should be given to recent advances in the mathematical modelling of the particle segregation and diffusion in fluid-saturated granular shear flows (Zhou et al., 2020; Cui et al., 2020, 2021, 2022). However, most of the published models tested against large-scale events use depth-averaged approximations derived from the vertical integration of the Navier–Stokes equations (Wu, 2007; Martínez-Aranda, 2021). At this point, it is worth distinguishing between the term "pore-pressure excess" or "dynamic pore-pore-pressure", which denotes the pressure deviation from its hydrostatic counterpart due to the relative movement between the solid and liquid phases, and the classical "non-hydrostatic contribution" in shallow water models due to the vertical flow acceleration (Castro-Orgaz and Hager, 2017), which is not considered in this work.

The simplest depth-averaged models assume a constant and uniform bulk density (single-phase approach), neglecting the changing composition of the fluidized material in the shallow-flow equations (Brufau et al., 2000; Murillo and García-Navarro, 2012; Luna et al., 2012; Ouyang et al., 2015a,b). Some of these single-phase models solely account for the effects of the pore-pressure in the frictional basal resistance using the Terzaghi's effective stress principle and including a uniform/constant ratio between the total normal stress and the pressure in the intergranular fluid (Hungr and McDougall, 2009; Martínez-Aranda et al., 2021; Denlinger and Iverson, 2001; Lancaster et al., 2003; Iverson and Denlinger, 2001; Pastor et al., 2015). A more realistic approach considers that this pore-pressure ratio can be time dependent due to the vertical self-consolidation of the aggregated material (Quecedo et al., 2004; Dewals et al., 2011). More complicated approaches solve the system of depth-averaged equations for the mass and momentum conservation of the liquid and solid phases separately (two-phase models) and include coupling terms between the phases (Meng and Wang, 2016; Li et al., 2018; Greco et al., 2019; Hess et al., 2019). Theoretically, these models should capture automatically the solid phase dilation phenomenon but there exists a high uncertainty in the estimation of the coupling terms between phases. Moreover, the appearance of numerical issues, mainly related to the loss of the hyperbolic character of the system, have hindered the application of these complete two-phase models to realistic debris flow problems (Pitman and Le, 2005; Kowalski, 2008; Pelanti et al., 2008).

An alternative approach consists of encapsulating the differences on the solid and fluid phases transport into the horizontal gradients of the depth-averaged composition. A few versions of this mixing-phase approach have been reported in last years (Fraccarollo et al., 2003; Armanini et al., 2009; Xia et al., 2018; Martínez-Aranda et al., 2021). George and Iverson (George and Iverson, 2011, 2014; Iverson and George, 2014) proposed a complete mixing-phase model solving the bulk mass and momentum equations of the fluidized material, supplemented with the mass conservation equation for the solid material. This model requires non-conservative coupling source terms between the bulk mass and the solid mass equations accounting by the dilation of solid volume fraction, which depends directly on the evolution of the pore-pressure within the flow column. The George and Iverson model provides a quadratic expression for the vertical distribution of pore-pressure along the flow column but it requires an additional convective equation for solving the basal pore-fluid pressure, including dissipation and forcing terms. Kowalski and McElwaine (2013) derived a mixing-phase model which includes the density changes into the convective fluxes by algebraically coupling the pore-pressure component of the stresses and the solid volume fraction, also differencing if there exists net solid phase settling or entrainment. Recently, Meyrat et al. (2022) proposed a mixing-layer approach computing the transport of one aggregated water-solid bottom layer plus a free fluid layer above it. This model coupled both layers using non-conservative source terms which account for the dilation of the aggregated solid skeleton in the bottom layer. Although the mixing-phase mathematical approach involves important simplifications of the flow physics, it shows a stable and controllable behaviour which represents a key feature to develop efficient predictive models suitable for realistic large-scale events.

In this work, we propose a novel mixing-layer approach for modelling the generation and persistence of shear-induced dynamic pressure within the pore-fluid in realistic water-sediment surface flows, and its influence on the dilation of the solid material and the flow mobility. This paper is structured as follow: Section 2 is devoted to the derivation and analysis of the governing equations for water-sediment flow, including dynamic pore-pressure; in Section 3 the depth-averaged 2D system of conservation laws for multi-grain mud and debris flows is introduced; the Finite-Volume numerical scheme used to solve the system is reported in Section 4; in Section 5 the proposed model is used to simulate synthetic test, laboratory experiments and real-scale mud/debris flows involving contractive and dilative behaviours; finally, the main conclusions are drawn in Section 6. As extra content, three appendix have been attached: the detailed derivation of the dilation term for the depth-averaged solid transport equation is included in Appendix A; further details on the conservative Finite Volume method are provided in Appendix B; and the fully-coupled Riemann solver used to compute the intercell flux for the numerical resolution of the equations is detailed in Appendix C.

2. Governing equations

In surface water-sediment flows, both solid and liquid phases are considered incompressible. However, the bulk fluidized material shows space and time variations depending on the local solid phase volumetric concentration, i.e. it behaves as a "compressible" material with variable density. Therefore, the local bulk density and the bulk linear momentum of the saturated fluidized material can be separated into phase contributions as

$$\rho = \rho_w(1-\phi) + \rho_s\phi \tag{1a}$$

$$\rho\mathbf{u} = \rho_w(1-\phi)\mathbf{u_w} + \rho_s\phi\mathbf{u_s} \tag{1b}$$

being ρ_s and ρ_w the density of the solid particles and the intergranular fluid respectively, ϕ the local volumetric solid concentration and $(1-\phi)$ the volumetric liquid phase fraction, i.e. the porosity of the sediment aggregate. The vector $\mathbf{u} = (u_x, u_y, u_z)$ is the local bulk velocity of the fluidized material in the global 3D reference system (x, y, z), with $\mathbf{u_w} = (u_{wx}, u_{wy}, u_{wz})$ the velocity of the pore-fluid and $\mathbf{u_s} = (u_{sx}, u_{sy}, u_{sz})$ the velocity of the sediment particles.

The movement of the water-sediment fluidized material is governed by the time-averaged Navier–Stokes equations for a density-variable water-sediment mixture flow, written as

$$\frac{\partial \rho}{\partial t} + \nabla \cdot (\rho \mathbf{u}) = 0 \tag{2a}$$

$$\frac{\partial \rho \mathbf{u}}{\partial t} + \nabla \cdot (\rho \mathbf{u} \otimes \mathbf{u}) = \rho \mathbf{g} - \nabla p + \nabla \cdot \boldsymbol{\tau} \tag{2b}$$

where $\mathbf{g} = (0, 0, -g)^T$, is the gravity vector, p denotes the pressure, $\boldsymbol{\tau}$ accounts for the bulk deviatoric shear stress tensor, $\nabla = \left(\frac{\partial}{\partial x}, \frac{\partial}{\partial y}, \frac{\partial}{\partial z}\right)$ is the 3D vector differential operator, and the time-averaged transport equations for the solid and liquid phases, expressed as

$$\frac{\partial \phi}{\partial t} + \nabla \cdot (\phi \mathbf{u}_\mathbf{s}) = 0 \tag{3a}$$

$$\frac{\partial (1-\phi)}{\partial t} + \nabla \cdot \left[(1-\phi)\mathbf{u}_\mathbf{w}\right] = 0 \tag{3b}$$

On the one hand, the convective solid transport in (3a) can be related to the bulk transport of the fluidized material as

$$\nabla \cdot (\phi \mathbf{u}_\mathbf{s}) = \nabla \cdot (\phi \mathbf{u}) - \nabla \cdot \left[\phi(\mathbf{u} - \mathbf{u}_\mathbf{s})\right] \tag{4}$$

where $\nabla \cdot \left[\phi(\mathbf{u} - \mathbf{u}_\mathbf{s})\right]$ represents the local deviation of the solid velocity with respect to the bulk flow velocity. This term is usually neglected in both suspended sediment transport and quasi-single phase models but, using (1a) and (1b), it can be rewritten as

$$\nabla \cdot \left[\phi(\mathbf{u} - \mathbf{u}_\mathbf{s})\right] = \nabla \cdot \left(\phi \frac{\rho_w}{\rho} \mathbf{q}_\mathbf{w}\right) \tag{5}$$

being $\mathbf{q}_\mathbf{w} = (1-\phi)(\mathbf{u}_\mathbf{w} - \mathbf{u}_\mathbf{s})$ the volumetric flux of intergranular fluid per unit area of bulk material, also referred to as specific discharge or Darcy's velocity in porous media theory (Haitjema and Anderson, 2016).

On the other hand, we define the local dilation rate of the solid phase as the divergence of the solid particle velocity $\nabla \cdot \mathbf{u}_\mathbf{s}$, which, operating (3a), can be related to the temporal evolution of the local solid volumetric concentration ϕ as

$$\nabla \cdot \mathbf{u}_\mathbf{s} = -\frac{1}{\phi} \frac{\mathrm{D}\phi}{\mathrm{D}t} \tag{6}$$

being $\mathrm{D}\phi/\mathrm{D}t = \partial\phi/\partial t + \mathbf{u}_\mathbf{s} \cdot \nabla\phi$ the material time derivative of the volumetric solid concentration (Iverson and George, 2014). Hence positive dilation rate is associated to porosity creation states, i.e. intergranular pores enlarge and the solid concentration reduces, and contrarily negative dilation rate is related to the contraction of the solid phase, i.e. increasing solid concentrations.

Furthermore, adding (3a) and (3b) allows to associate the local dilation rate to the intergranular fluid flux per unit flow area, i.e the specific discharge $\mathbf{q}_\mathbf{w}$, as

$$\nabla \cdot \mathbf{u}_\mathbf{s} = \nabla \cdot \left[(1-\phi)(\mathbf{u}_\mathbf{s} - \mathbf{u}_\mathbf{w})\right] = -\nabla \cdot \mathbf{q}_\mathbf{w} \tag{7}$$

indicating that porosity creation (positive dilation rate) is accompanied by a local influx of fluid which fills the enlarging pores and, contrarily, porosity contraction (negative dilation rate) is balanced by a local intergranular fluid outflux, leading to a denser packed aggregated material (Fig. 1).

In order to derive a reliable mathematical closure linking the differential movements of the intergranular fluid and the solid aggregate, we combine two well-established concepts from the granular-flow mechanics and the porous media theory:

(a) Neglecting the self-consolidation due to normal stresses, the granular-flow mechanics allows to estimate the shear-induced dilation rate of the solid aggregate under quasi-steady shear states as

$$\nabla \cdot \mathbf{u}_\mathbf{s} = \dot{\gamma} \tan\psi \tag{8}$$

where $\dot{\gamma}$ is the macroscopic shear rate and ψ accounts for the shear-induced dilatancy, a state-dependent property of the granular aggregate usually expressed as an angle ($-\pi/2 \leq \psi \leq \pi/2$).

Considering a steady shear state, i.e. $\dot{\gamma} = \text{const} \neq 0$, if the dilatancy angle ψ is assumed constant in time, the closure relation (8) causes the solid dilation rate remains also constant in time and hence (6) leads to the unbounded evolution of the solid concentration. This simple theoretical test demonstrates that the shear-induced dilatancy angle ψ cannot be constant and it should evolve with the local conditions of the fluidized material. Forterre and Pouliquen (2008) and Pailha and Pouliquen (2009) proposed a linear dependency of the dilatancy $\tan\psi$ on the bulk solid concentration ϕ as

$$\tan\psi = k_1(\phi - \phi_{eq}) \tag{9}$$

being k_1 a positive tuning coefficient, which should be calibrated for each specific application, and ϕ_{eq} an equilibrium value of the bulk solid concentration that balances the local stress and the shear rate. The equilibrium concentration ϕ_{eq} reduces monotonically as the normal stress decreases and the shear rate increases (Iverson and George, 2014; Martínez-Aranda, 2021). For the sake of simplicity, in this work ϕ_{eq} is considered constant, but to include its dependence with the local stress state is retained as a future model improvement.

(b) Porous media theory relates the liquid-phase movement within the granular aggregate to the local gradients of pore-fluid pressure. Estimation of the intergranular fluid pressure distribution along the flow column $\mathcal{P}(z)$ is a challenging task for modelling multi-phase surface flows (Iverson, 1997; Iverson and Vallance, 2001; Jakob and Hungr, 2005), although its effects on the reduction of the effective shear stress between solid grains seem to be demonstrated (Major and Iverson, 1999; Berti et al., 1999; Berti and Simoni, 2005; McArdell et al., 2007; Iverson et al., 2011). The intergranular fluid pressure can be separated into its hydrostatic part $p_h(z) = \rho_w g(z_s - z)$, with z_s the flow free surface level, plus a local pressure excess $p_e(z)$ (also known as dynamic pore pressure), hence $\mathcal{P}(z) = p_h(z) + p_e(z)$. Following Denlinger and Iverson (2001), Lancaster et al. (2003), Iverson et al. (2010) and Ouyang et al. (2015a), the dynamic component $p_e(z)$ is here expressed as a fraction of the hydrostatic pressure as

$$p_e(z) = \mathcal{E}\rho_w g(z_s - z) \tag{10}$$

being $\mathcal{E}$ positive for total pore pressure higher than the hydrostatic and negative when total pore pressure is lower than the hydrostatic value. The Darcy Law relates the specific discharge to the dynamic pressure gradients within the intergranular fluid as

$$\mathbf{q}_\mathbf{w} = -\frac{\kappa}{\mu} \nabla p_e \tag{11}$$

where κ is the hydraulic permeability of the solid aggregate and μ denotes the molecular viscosity of the intergranular fluid. Therefore, the Darcy Law indicates that, in a porous medium, the intergranular fluid moves from high-pressure to low-pressure zones with a relative velocity which depends on both the permeability of the medium and the fluid viscosity (Whitaker, 1986).

Then, replacing (8) and (11) into (7) leads to

$$\dot{\gamma} \tan\psi = \nabla \cdot \left(\frac{\kappa}{\mu} \nabla p_e\right) \tag{12}$$

and assuming the shallow-flow scaling $H \ll L$, being H the characteristic flow depth and L the characteristic horizontal length, allows to assess $\partial^2/\partial x^2 \ll \partial^2/\partial z^2$, since $\partial^2/\partial x^2$ scales with $1/L^2$ whereas $\partial^2/\partial z^2$ scales with $1/H^2$ (Iverson and George, 2014). Therefore, the derivative terms along the horizontal x- and y-coordinates can be neglected.

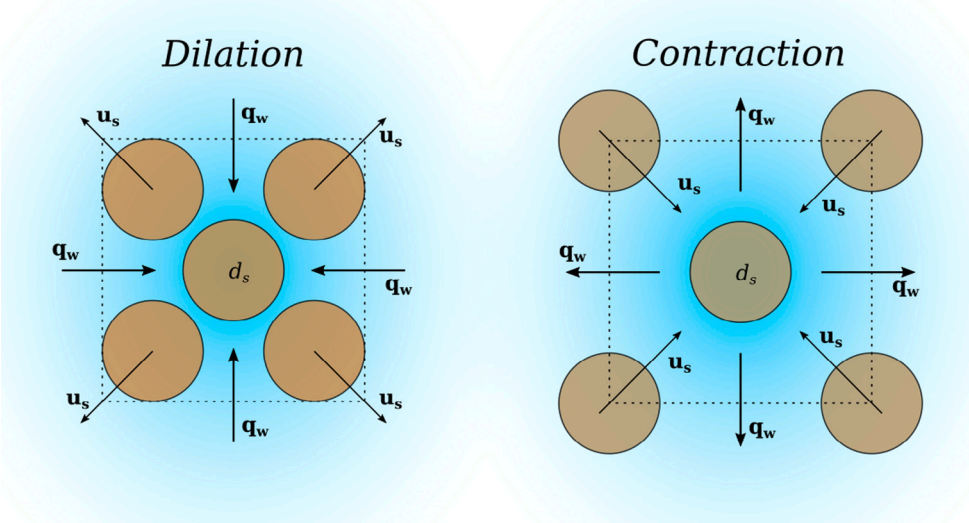

Fig. 1. Balance of dilation rate and intergranular fluid flux for (left) porosity creation states and (right) solid-phase contraction states.

Furthermore, assuming that local κ/μ value remains constant along the vertical direction allows (12) to reduce to the second-order equation

$$\frac{\partial^2 p_e}{\partial z^2} = \frac{\mu}{\kappa}\dot{\gamma}\tan\psi = \text{const} \tag{13}$$

and integrating twice along the flow thickness leads to

$$p_e(z) = \frac{\mu}{2\kappa}\dot{\gamma}\tan\psi(z - z_b)^2 + A(z - z_b) + B \tag{14}$$

being A and B two integration constants.

To impose boundary conditions to (14), we assume that the intergranular fluid pressure takes the atmospheric value at the free surface, i.e. $p_e(z_s) = 0$. Furthermore, we impose that the dynamic pressure at the bed surface can be expressed as $p_e(z_b) = \mathcal{E}_b\rho_w g h$, being $\mathcal{E}_b$ a dimensionless factor to express the basal dynamic pressure as a fraction of the hydrostatic value. Moreover, we consider that the solid and fluid velocities at the bed level are equal (non-penetration condition) and hence the specific discharge $\mathbf{q_w}$ throughout the bed surface is null. Therefore, using (11), we can also impose $\partial p_e/\partial z = 0$ at the bed surface z_b. Assuming these three boundary conditions, the dynamic component of the intergranular fluid pressure along the flow column must satisfy the quadratic expression

$$p_e(z) = \frac{\mu}{2\kappa}\dot{\gamma}\tan\psi(z - z_b)^2 + \mathcal{E}_b\rho_w g h \tag{15}$$

being $\dot{\gamma} = 2|\mathbf{u}|/h$ the depth-averaged macroscopic shear rate and $\mathcal{E}_b$ the basal dynamic pore-pressure parameter

$$\mathcal{E}_b = \frac{-\mu h}{2\kappa\rho_w g}\dot{\gamma}\tan\psi \tag{16}$$

This closure (15)–(16) indicates that the dynamic pressure within the intergranular fluid depends on both the flow shear rate and the dilatancy state of the solid aggregate. We can analyse the behaviour of the pore-fluid pressure separately:

- First, considering a constant shear rate in the dilatancy relationship (9), the pore pressure distribution along the vertical coordinate is hydrostatic for $\phi = \phi_{eq}$, representing the null dilatancy state. Then, as the actual solid concentration ϕ diverges from the equilibrium lithostatic value ϕ_{eq}, the pore pressure distribution separates from the hydrostatic linear profile since the positive/negative dilatancy $\tan\psi$ is enhanced. Solid concentrations larger than the equilibrium ϕ_{eq} lead to pore pressures lower than the hydrostatic value, i.e. the granular behaviour dominates the flow, whereas solid concentrations lower than ϕ_{eq} cause the pore pressure to increase over the hydrostatic value, leading to a more liquefied behaviour.

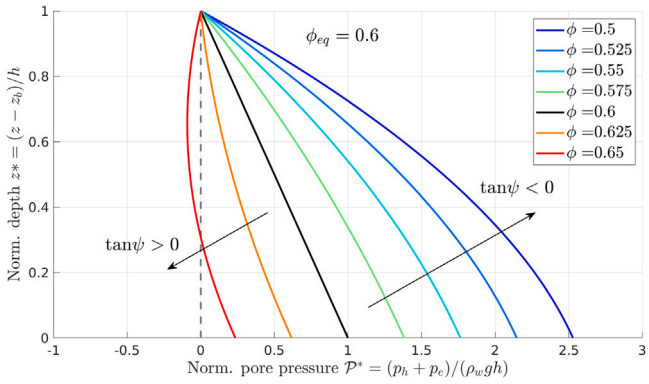

Fig. 2. Normalized pore-fluid pressure $\mathcal{P}^*(z)$ along the normalized flow depth z^* as a function of the solid volumetric concentration ϕ, for a constant shearing-state setting $\mu = 10^{-3}$ Pa · s, $\kappa = 10^{-8}$ m^2 $h = 10$ m, $\dot{\gamma} = 6\,\text{s}^{-1}$, $\phi_{eq} = 0.6$, $k_1 = 0.05$, $\rho_w = 1000\,\text{kgm}^{-3}$ and $g = 9.81\,\text{ms}^{-2}$.

Fig. 2 shows the evolution of the normalized pore-fluid pressure $\mathcal{P}^*(z) = \mathcal{P}(z)/(\rho_w g h)$ along the normalized flow depth $z^* = (z - z_b)/h$ as the solid concentration ϕ diverges from the ϕ_{eq} value, considering constant shear rate. Positive values of the dynamic pore pressure p_e, i.e. an intergranular fluid pressure $\mathcal{P}$ higher than the hydrostatic p_h, denote negative dilatancy states $\tan\psi < 0$ and hence to porosity destruction processes. Contrarily, negative value of the dynamic pore pressure p_e, i.e. an intergranular fluid pressure $\mathcal{P}$ lower than the hydrostatic p_h, are related to positive dilatancy states $\tan\psi > 0$ and porosity creation processes.

- Second, (15) also indicates that the behaviour of the dynamic pore pressure depends on the shear rate. Fig. 3 depicts the evolution of the normalized intergranular fluid pressure $\mathcal{P}^*(z)$ along the normalized flow depth z^* as the depth-averaged shear rate $\dot{\gamma}$ increases, considering both positive and negative dilatancy states. Note that the pore pressure is fully hydrostatic for the quiescent lithostatic case $\dot{\gamma} = 0$. For constant positive dilatancy $\tan\psi > 0$, the higher the shear rate, the larger the negative deviation of the pore pressure $\mathcal{P}(z)$ respect to the hydrostatic profile. Contrarily, under a constant negative dilatancy state $\tan\psi < 0$, higher shear rates lead to larger positive deviations of the pore pressure $\mathcal{P}(z)$ respect to the hydrostatic linear profile.

The pore-pressure distribution along the vertical coordinate $\mathcal{P}(z) = p_h(z) + p_e(z)$, estimated using the closure relations (15)–(16), follows

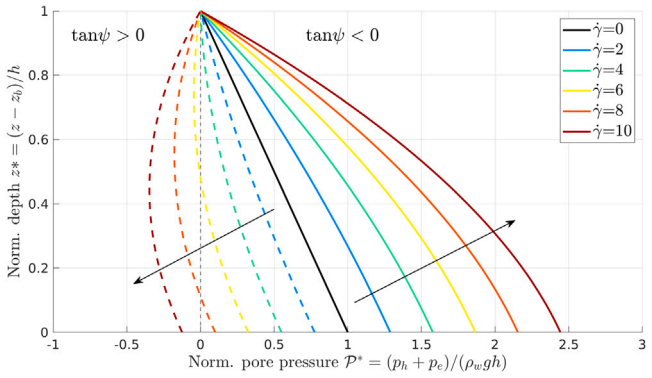

Fig. 3. Normalized pore-fluid pressure $\mathcal{P}^*(z)$ along the normalized flow depth z^* as a function of the shearing-state, setting $\mu = 10^{-3}$ Pa · s, $\kappa = 10^{-8}$ m^2, $h = 10$ m, $k_1 = 0.05$, $\rho_w = 1000$ kgm^{-3}, $g = 9.81$ ms^{-2}, $\phi_{eq} = 0.6$ and assuming a constant solid concentration $\phi = 0.55$ (negative dilatancy)–$\phi = 0.65$ (positive dilatancy).

the same behaviour as that reported by George and Iverson (George and Iverson, 2011; Iverson and George, 2014). The closure relationship (15)–(16) allows to estimate the dynamic pore pressure $p_e(z)$ directly from the local flow features and the dilatancy state of the solid aggregate. Contrarily, George and Iverson reported an almost similar quadratic expression for the evolution of the pore-pressure $\mathcal{P}(z)$ along the flow column, but their model required to solve an additional advection–diffusion equation for the basal pore-fluid pressure value, including dominant source terms, which increased the model complexity and uncertainty. Furthermore, Bouchut et al. (2016) proposed also an explicit expression for the excess of pore pressure depending on the dilatancy angle ψ of the solid phase and the shear strain $\dot{\gamma}$ of the fluidized material. Bouchut et al. derived this dynamic contribution to the hydrostatic pressure starting from the normal velocity differences between the solid and liquid phases. They achieved an expression which included terms depending on the depth-averaged horizontal gradients of the normal velocity differences but with the same quadratic behaviour as that reported here, ranging from a maximum basal dynamic pore-pressure value to a negligible pressure at the mixture top surface. Pailha and Pouliquen (2009) also reported a relationship for the excess of pore pressure depending on the dilatancy angle ψ and the shear strain $\dot{\gamma}$ for submerged granular avalanches which is a particular case of the Bouchut et al. model.

2.1. Stress partition

The conventional stress partitioning in surface flow involving dense-packed water-sediment aggregates considers that the 3 × 3 bulk deviatoric stress tensor $\boldsymbol{\tau}$ in the momentum equation (2b) is composed of a frictional tensor $\boldsymbol{\tau_f}$, accounting for the shear stress between solid particles, plus a viscous tensor $\boldsymbol{\tau_v}$, which accounts for the shear stress in the intergranular fluid (Pastor et al., 2015). Therefore $\boldsymbol{\tau} = \boldsymbol{\tau_f} + \boldsymbol{\tau_v}$ and, assuming a simple-shear flow within the column, it can be written as

$$\boldsymbol{\tau} = \begin{pmatrix} 0 & 0 & (\tau_f + \tau_v)\,\hat{u}_x \\ 0 & 0 & (\tau_f + \tau_v)\,\hat{u}_y \\ (\tau_f + \tau_v)\,\hat{u}_x & (\tau_f + \tau_v)\,\hat{u}_y & 0 \end{pmatrix} \tag{17}$$

where $(\hat{u}_x, \hat{u}_y)$ denotes the components of the flow direction unit vector along the horizontal x- and y-coordinates. The shear stress within the pore fluid $\tau_v(z)$ is usually assumed pure viscous or turbulent for free-surface mud/debris flows, whereas the frictional component $\tau_f(z)$ is here estimated by the Coulomb-Terzaghi relation as

$$\tau_f(z) = \sigma_e(z)\,\tan\delta_f = \left[\sigma(z) - \mathcal{P}(z)\right]\tan\delta_f \tag{18}$$

where $\sigma_e(z) = \sigma(z) - \mathcal{P}(z)$ is the effective normal stress within the solid aggregate, $\sigma(z)$ denotes the total normal stress along the vertical coordinate and δ_f is the effective friction angle of solid grains under non-zero dilatancy (Jakob and Hungr, 2005). Estimating the vertical profile of total normal stress as $\sigma(z) = \rho g(z_s - z)$, the shear stress distribution along the flow column could be expressed as

$$\tau(z) = \left[(\rho - \rho_w)g(z_s - z) - p_e(z)\right]\tan\delta_f + \tau_v(z) \tag{19}$$

and hence the dynamic pressure in the intergranular fluid $p_e(z)$ changes the frictional shear stress between the sediment grains, affecting the macroscopic mobility of the fluidized material and the flow runout distance. It is worth noting that, when the pore pressure exceeds the total normal stress, i.e $\mathcal{P}(z) \geq \sigma(z)$, the effective normal stress $\sigma_e(z)$ becomes negligible and the material is fully-liquefied with null frictional shear stress $\tau_f = 0$.

More complex approaches can be found in literature to include the effects of the solid phase dilation/contraction in the frictional shear stress between grains. A widespread approach is based on considering an additional contribution to the grain shear stress, hence the effective state-dependent friction coefficient is expressed as $\tan\delta_{eff} = \tan\delta_f + \tan\psi$ (Pailha and Pouliquen, 2009; Bouchut et al., 2016; Heyman et al., 2017). An alternative approach is to consider the dilatancy effects as changes in the total solid-phase pressure, which depends on the visco-elasto-plastic response of the material and takes into account the plastic effects due to particle rearrangements (Montellà et al., 2021; Mari et al., 2014; Lee, 2021).

3. 2D depth-averaged model for water-sediment shallow flows

The 2D model for density-variable water-sediment shallow flows involves the integration along the flow depth of the 3D equations for mass and linear momentum conservation of the bulk fluidized material, (2a) and (2b). This leads to the continuity equation for the fluidized mass

$$\frac{\partial(\overline{\rho}h)}{\partial t} + \frac{\partial}{\partial x}\left(\overline{\rho}h\overline{u}\right) + \frac{\partial}{\partial y}\left(\overline{\rho}h\overline{v}\right) = 0 \tag{20}$$

and the conservation laws for the bulk linear momentum along the x- and y-coordinates, expressed as

$$\frac{\partial(\overline{\rho}h\overline{u})}{\partial t} + \frac{\partial}{\partial x}\left(\overline{\rho}h\overline{u}^2 + \frac{1}{2}g\overline{\rho}h^2\right) + \frac{\partial}{\partial y}\left(\overline{\rho}h\overline{u}\,\overline{v}\right) = -g\overline{\rho}h\frac{\partial z_b}{\partial x} - \tau_{bx} \tag{21a}$$

$$\frac{\partial(\overline{\rho}h\overline{v})}{\partial t} + \frac{\partial}{\partial x}\left(\overline{\rho}h\overline{u}\,\overline{v}\right) + \frac{\partial}{\partial y}\left(\overline{\rho}h\overline{v}^2 + \frac{1}{2}g\overline{\rho}h^2\right) = -g\overline{\rho}h\frac{\partial z_b}{\partial y} - \tau_{by} \tag{21b}$$

being h the vertical flow depth, $\overline{\rho}$ the depth-averaged bulk density, $(\overline{u}, \overline{v})$ the depth-averaged flow velocity along the x- and y-coordinates, z_b the bed layer elevation, g the gravity acceleration and (τ_{bx}, τ_{by}) the components of the basal resistance $\boldsymbol{\tau_b}$ along the x- and y-coordinates. Note that, for the sake of simplicity, the mass exchange between the flow and the bed layer has been neglected in (20), as well as both the dispersive and the turbulent depth-averaged stress terms in the momentum equations (21). The detailed integration of these three conservation laws along the flow depth can be found in Martínez-Aranda (2021).

In the work, the basal resistance $\boldsymbol{\tau_b}$ is expressed as

$$\boldsymbol{\tau_b} = (\tau_{bx}, \tau_{by}) = \tau_b\,\mathbf{n_u} \tag{22}$$

being τ_b the basal shear stress, $\mathbf{n_u} = (n_{ux}, n_{uy}) = (\overline{u}, \overline{v})/\mathcal{U}$ the velocity unit vector and $\mathcal{U} = \sqrt{\overline{u}^2 + \overline{v}^2}$ the modulus of the depth-averaged bulk velocity.

To close, different hybrid formulations have been proposed for the depth-averaged basal resistance term. Based on (19), the most widespread strategy for granular turbulent flows, where the frictional stress between grains dominates at low shear rates, consists of the combination of the grain frictional stress and the turbulent Manning roughness approach to estimate the total basal resistance as

$$\tau_b = \tau_{fb} + \overline{\rho}g\frac{n_b^2\,\mathcal{U}^2}{h^{1/3}} \tag{23}$$

where τ_{fb} is the frictional yield strength at the basal surface and n_b the Manning roughness parameter (O'Brien et al., 1993; Juez et al., 2014; Xia et al., 2018; Li et al., 2018; Martínez-Aranda et al., 2021). The frictional yield strength τ_{fb} is estimated using a Coulomb-Terzaghi expression relating the grain frictional shear stress to the effective normal stress at the basal surface as

$$\tau_{fb} = \left(\overline{\rho} g h - \mathcal{P}_b\right) \tan \delta_f \tag{24}$$

where δ_f is the frictional angle for the solid phase and $\mathcal{P}_b$ is the pore-fluid pressure at the bed surface, written as

$$\mathcal{P}_b \equiv \mathcal{P}(z_b) = (1 + \mathcal{E}_b)\rho_w g h \tag{25}$$

being $\mathcal{E}_b$ the basal dynamic pore-pressure factor (16). It is worth mentioning that, for the limiting case where the basal dynamic pore-pressure factor satisfies $\mathcal{E}_b \geq (\overline{\rho}/\rho_w - 1)$, the pore pressure $\mathcal{P}_b$ balances the total normal stress at the bed surface, i.e. $\overline{\rho} g h$, hence the material is fully-liquefied and the frictional resistance at the bed becomes null.

The solid phase is composed by multiple sediment classes with different characteristic particle diameter d_{sp}, solid density ρ_{sp} and volumetric concentration ϕ_p. Using (3a), (4) and (5), the 3D time-averaged mass conservation equation for the pth sediment class can be written as

$$\frac{\partial \phi_p}{\partial t} + \nabla \cdot (\phi_p \mathbf{u}) = \nabla \cdot \left(\phi_p \frac{\rho_w}{\rho} \mathbf{q_w}\right) \tag{26}$$

where the source term on the right hand side represents the drag effects exerted by the specific discharge $\mathbf{q_w}$ on the convective solid flux. The transport equation (26) is also integrated along the entire flow column using the Leibnitz's rule (Martínez-Aranda, 2021), leading to

$$\frac{\partial (h\overline{\phi}_p)}{\partial t} + \frac{\partial}{\partial x}\left(h\overline{u}\overline{\phi}_p\right) + \frac{\partial}{\partial y}\left(h\overline{v}\overline{\phi}_p\right) = \int_{z_b}^{z_s} \nabla \cdot \left(\phi_p \frac{\rho_w}{\rho} \mathbf{q_w}\right) \mathrm{d}z \tag{27}$$

where $\overline{\phi}_p$ is the depth-averaged concentration of the pth sediment class along the flow column.

The non-conservative source term on the right hand side of Eq. (27) is associated to the porosity increase/decrease caused by the shear-induced dilation of the solid aggregate during the movement of the fluidized material (Iverson and George, 2014). Integrating this dilation drag term along the flow depth requires to impose boundary conditions for the specific discharge $\mathbf{q_w}$ at the fixed bed surface boundary z_b and at the flow free surface z_s, but allows to transform this non-conservative source term into a conservative deviatoric contribution to the convective solid flux depending on the pore-fluid pressure gradient. The resulting depth-averaged transport equation for the pth sediment class (27) reads

$$\frac{\partial (h\overline{\phi}_p)}{\partial t} + \frac{\partial}{\partial x}\left(h\overline{u}\overline{\phi}_p + \mathcal{L}_x \frac{\rho_w}{\overline{\rho}}\overline{\phi}_p\right) + \frac{\partial}{\partial y}\left(h\overline{v}\overline{\phi}_p + \mathcal{L}_y \frac{\rho_w}{\overline{\rho}}\overline{\phi}_p\right) = 0 \tag{28}$$

where $\mathcal{L}_x$ and $\mathcal{L}_y$ are the deviatoric dilation fluxes along the x- and y-coordinates, respectively, expressed as

$$\mathcal{L}_x = \frac{\kappa}{\mu}\left(\frac{\partial \mathcal{P}_e}{\partial x} + \mathcal{E}_b \rho_w g h \frac{\partial z_b}{\partial x}\right) \qquad \mathcal{L}_y = \frac{\kappa}{\mu}\left(\frac{\partial \mathcal{P}_e}{\partial y} + \mathcal{E}_b \rho_w g h \frac{\partial z_b}{\partial y}\right) \tag{29}$$

being $\mathcal{E}_b = \frac{-\mu h}{2\kappa \rho_w g}\dot{\gamma} \tan\psi$ the basal dynamic pore pressure parameter (16) and $\mathcal{P}_e = \frac{-\mu h^3}{3\kappa}\dot{\gamma} \tan\psi$ the integral of the dynamic pore pressure $p_e(z)$ along the flow column (A.6). Details on the derivation of this solid dilation flux can be found in Appendix A.

Therefore, the depth-averaged bulk density of the fluidized material can be related to the multi-grain solid concentration as

$$\overline{\rho} = \rho_w + \sum_{p=1}^{\mathrm{NS}} (\rho_{sp} - \rho_w)\overline{\phi}_p = \rho_w (1 + \overline{\chi}) = \rho_w \overline{r} \tag{30}$$

where $\overline{\chi} = \sum_{p=1}^{\mathrm{NS}} (r_{sp} - 1)\overline{\phi}_p$ is referred to as the depth-averaged buoyant solid concentration, being $r_{sp} = \rho_{sp}/\rho_w$ the normalized solid density for the pth sediment class, NS is the number of sediment classes and

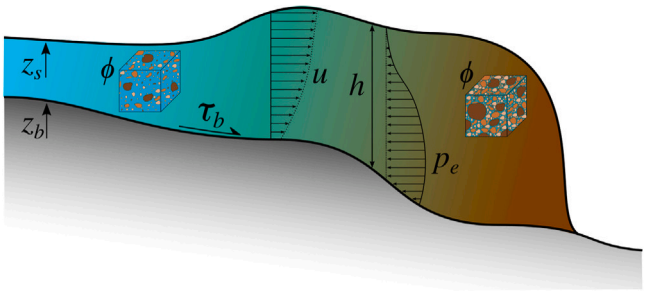

Fig. 4. Main variables involved in the density-variable water-sediment flow.

$\overline{r} = 1 + \overline{\chi}$ is the normalized bulk density of the fluidized material along the flow column. Fig. 4 shows a sketch with the main physical variables involved in the governing equations used for modelling density-variable water-sediment flows over fixed beds.

The resulting 2D system of equations is composed by four conservation laws accounting for the bulk mass (20), the bulk linear momentum (21a)–(21b) along the x- and y-coordinates respectively, and the multi-grain solid mass combining (28) and (30). The system can be recast in vector form as

$$\frac{\partial \mathbf{U}}{\partial t} + \nabla \cdot \mathbf{E}(\mathbf{U}) + \nabla \cdot \mathbf{L}(\mathbf{U}) = \mathbf{S_b}(\mathbf{U}) + \mathbf{S_\tau}(\mathbf{U}) \tag{31}$$

where $\mathbf{U}$ is the vector of conservative variables

$$\mathbf{U} = \left(\begin{array}{cccc} \overline{r}h, & \overline{r}h\overline{u}, & \overline{r}h\overline{v}, & h\overline{\chi} \end{array} \right)^T \tag{32}$$

and $\mathbf{E}(\mathbf{U}) = \left[\mathbf{F}(\mathbf{U}), \mathbf{G}(\mathbf{U})\right]$ are the convective fluxes along the x- and y-coordinates

$$\mathbf{F}(\mathbf{U}) = \begin{pmatrix} \overline{r}h\overline{u} \\ \overline{r}h\overline{u}^2 + \frac{1}{2}g\overline{r}h^2 \\ \overline{r}h\overline{u}\,\overline{v} \\ h\overline{u}\,\overline{\chi} \end{pmatrix} \qquad \mathbf{G}(\mathbf{U}) = \begin{pmatrix} \overline{r}h\overline{v} \\ \overline{r}h\overline{u}\,\overline{v} \\ \overline{r}h\overline{v}^2 + \frac{1}{2}g\overline{r}h^2 \\ h\overline{v}\,\overline{\chi} \end{pmatrix} \tag{33}$$

being $\nabla = \left(\frac{\partial}{\partial x}, \frac{\partial}{\partial y}\right)$. It is worth noting that the normalized bulk density $\overline{r}$, the flow depth h, the flow velocity components $(\overline{u}, \overline{v})$, and the bulk buoyant solid concentration $\overline{\chi}$ are coupled in the conservative variables and conservative fluxes on the left hand side of (31).

The term $\mathbf{L}(\mathbf{U}) = \left[\mathbf{L_x}(\mathbf{U}), \mathbf{L_y}(\mathbf{U})\right]$ involves the deviatoric solid flux caused by the shear-induced dilation of the sediment phase

$$\mathbf{L_x}(\mathbf{U}) = \begin{pmatrix} 0 \\ 0 \\ 0 \\ \mathcal{L}_x \frac{\overline{\chi}}{\overline{r}} \end{pmatrix} \qquad \mathbf{L_y}(\mathbf{U}) = \begin{pmatrix} 0 \\ 0 \\ 0 \\ \mathcal{L}_y \frac{\overline{\chi}}{\overline{r}} \end{pmatrix} \tag{34}$$

being $(\mathcal{L}_x, \mathcal{L}_y)$ the dilation-induced deviatoric flux (29) along the x- and y-coordinate respectively.

The vector $\mathbf{S_b}(\mathbf{U})$ denotes the momentum source term associated to the pressure force variation on the bed interface, whereas the vector $\mathbf{S_\tau}(\mathbf{U})$ accounts for the momentum dissipation due to the basal resistance term, written as

$$\mathbf{S_b}(\mathbf{U}) = \begin{pmatrix} 0 \\ -g\overline{r}h\frac{\partial z_b}{\partial x} \\ -g\overline{r}h\frac{\partial z_b}{\partial y} \\ 0 \end{pmatrix} \qquad \mathbf{S_\tau}(\mathbf{U}) = \begin{pmatrix} 0 \\ -\frac{\tau_b}{\rho_w} n_{ux} \\ -\frac{\tau_b}{\rho_w} n_{uy} \\ 0 \end{pmatrix} \tag{35}$$

where τ_b is the frictional-turbulent basal shear stress (23). It is worth noting that this model is specially designed for highly transient flows of sediment-laden non-Newtonian materials with noticeable density gradients, as occurs in real-scale densely-packed mud and debris flows (Martínez-Aranda et al., 2021).

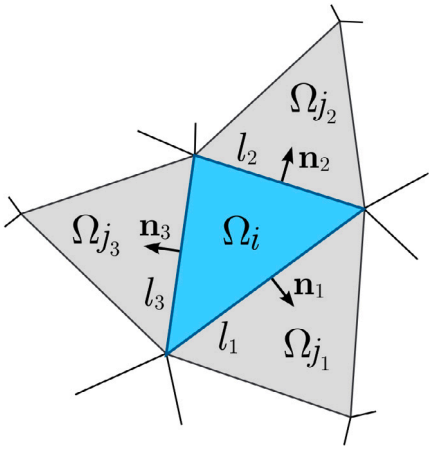

Fig. 5. Computational cells in unstructured meshes.

4. Finite volume method

In this section, the derivation of a Finite Volume (FV) numerical scheme for 2D density-variable shallow flow is summarized. System (31) is non-linear, time dependent, contains momentum source terms and it belongs to the hyperbolic class. For the sake of clarity, the upper bar over the depth-averaged variables is suppressed from now on. Following the FV method, the spatial domain is discretized in computational cells with an arbitrary number of edges, creating a fixed-in-time computational mesh. Then, assuming piecewise uniform flow variables at each cell and applying the Gauss theorem to the flux term, system (31) is integrated in each cell Ω_i as

$$\frac{\mathrm{d}}{\mathrm{d}t}\int_{\Omega_i}\mathbf{U}\,\mathrm{d}\Omega+\sum_{k=1}^{\mathrm{NE}}(\mathbf{E}\cdot\mathbf{n})_k\,l_k=\int_{\Omega_i}\mathbf{S_b}(\mathbf{U})\,\mathrm{d}\Omega+\int_{\Omega_i}\mathbf{S_\tau}(\mathbf{U})\,\mathrm{d}\Omega-\sum_{k=1}^{\mathrm{NE}}(\mathbf{L}\cdot\mathbf{n})_k\,l_k \tag{36}$$

being $(\mathbf{E}\cdot\mathbf{n})_k$ the normal conservative flux throughout the kth edge, $\mathbf{n}_k$ and l_k the corresponding outward unit normal vector and the edge length, respectively, and NE the number of edges for the i cell (Fig. 5), which could be arbitrary.

At each edge, the local coordinates are defined following the normal $\mathbf{n}_k = (n_x, n_y)_k$ and tangential $\mathbf{t}_k = (-n_y, n_x)_k$ unit vectors, and the system (36) is integrated ensuring that the rotation invariant property is satisfied for all terms, including the non-Newtonian bed shear resistance (Godlewski and Raviart, 1996; Toro, 1997; Martínez-Aranda et al., 2022). Then, assuming a piecewise uniform value of the conservative variables $\mathbf{U}$ for the i cell at each time $t = t^n$ and using first-order explicit temporal integration, the value of the conservative variables $\mathbf{U}$ can be updated to the next time $t = t^{n+1}$ as

$$\mathbf{U}_i^{n+1}=\mathbf{U}_i^{n}-\frac{\Delta t}{A_i}\sum_{k=1}^{\mathrm{NE}}\mathbf{R}_k^{-1}\,\boldsymbol{\mathcal{F}}_k^{\downarrow}\,l_k \tag{37}$$

being A_i the discrete cell area, $\Delta t = t^{n+1} - t^n$ the time step and $\mathbf{R}_k^{-1}$ the inverse of the 4×4 rotation matrix $\mathbf{R}_k$ at the kth cell edge. The vector $\boldsymbol{\mathcal{F}}_k^{\downarrow}$ denotes the normal explicit upwind flux through the kth cell edge

$$\boldsymbol{\mathcal{F}}_k^{\downarrow}=\boldsymbol{F}_k^{\downarrow-}+\mathbf{L}_{\mathbf{n}k}^{\downarrow-} \tag{38}$$

including the augmented flux $\boldsymbol{F}_k^{\downarrow-}$, consisting of the conservative edge fluxes plus the bed-pressure contribution plus the basal resistance split term, supplemented by the deviatoric dilation-related contribution to the solid flux $\mathbf{L}_{\mathbf{n}k}^{\downarrow-}$. Further details on the derivation of the Finite Volume (FV) method for unstructured meshes, satisfying the rotation invariant property for arbitrary number-of-edges cells, can be found in Appendix B.

4.1. Flux computation and flow features reconstruction

In this work, the augmented upwind flux $\boldsymbol{F}_k^{\downarrow-}$ is computed using the approximate Riemann problem (RP) theory and a first-order Roe's solver for density-variable shallow flows. Details on the flux computation have been extensively reported in Martínez-Aranda et al. (2020), Martínez-Aranda (2021) and Martínez-Aranda et al. (2021). For the sake of completeness, a summary of the flux solver is included in Appendix C. Therefore, $\boldsymbol{F}_k^{\downarrow-}$ at the kth cell edge is computed as

$$\boldsymbol{F}_k^{\downarrow-}=\mathbf{F}(\hat{\mathbf{U}}_i^n)+\sum_{m-}\left[(\widetilde{\lambda}_m\widetilde{\alpha}_m-\widetilde{\beta}_m-\widetilde{\sigma}_m)\widetilde{\mathbf{e}}_m\right]_k^n \tag{39}$$

where the vector $\mathbf{F}(\hat{\mathbf{U}}_i^n)$ denotes the homogeneous normal fluxes, being $\hat{\mathbf{U}}_i^n = \mathbf{R}_k\mathbf{U}_i^n$ the conservative variables expressed in local reference system of the kth cell edge. The terms $\widetilde{\lambda}_{m,k}$ are the wave celerities at the edge, i.e. the eigenvalues of the Jacobian matrix of the RP, $(\widetilde{\mathbf{e}}_m)_k$ are the eigenvectors of the RP, $\widetilde{\alpha}_{m,k}$ denote the wave strengths accounting for the discontinuity on the conservative variables, $\widetilde{\beta}_{m,k}$ are the source strengths which include the integrated bed pressure through the cell edge and the coefficients $\widetilde{\sigma}_{m,k}$ are the source strengths accounting for the split basal resistance contribution at the cell edge. The subscript $m-$ under the sums indicate that only the waves travelling inward the i cell are considered, leading to the upwind computation of the flux at the edge, whereas superscripts $\widetilde{}$ indicate edge-averaged quantities of the variables.

The deviatoric solid dilation contribution to the intercell flux at the kth edge, $\mathbf{L}_{\mathbf{n}k}^{\downarrow-}$, is computed using a first-order upwind approximation as

$$\mathbf{L}_{\mathbf{n}k}^{\downarrow-}=\begin{pmatrix}0\\0\\0\\\widetilde{\mathcal{L}}_{nk}\left(\frac{\chi}{r}\right)_{\{upw\}}^{n}\end{pmatrix}\quad\text{with}:\begin{cases}\{upw\}=i & \text{if}\quad \boldsymbol{\mathcal{F}}_k^{\{1\}\downarrow}\geq 0\\ \{upw\}=j & \text{if}\quad \boldsymbol{\mathcal{F}}_k^{\{1\}\downarrow}<0\end{cases} \tag{40}$$

being $\widetilde{\mathcal{L}}_{nk}$ the edge-averaged value of the deviatoric dilation-relation contribution at the kth cell edge, computed as

$$\widetilde{\mathcal{L}}_{nk}=\left[\frac{\widetilde{\kappa}}{\widetilde{\mu}}\left(\frac{\Delta\mathcal{P}_e}{d_n}+\widetilde{\mathcal{E}}_b\rho_w g\widetilde{h}\frac{\Delta z_b}{d_n}\right)\right]_k \tag{41}$$

with $\Delta\mathcal{P}_e$ and Δz_b accounting for the discontinuity of the integrated dynamic pore pressure and the bed level at the edge respectively, d_n denoting the normal-distance between cell centres and the superscripts $\widetilde{}$ indicating edge-averaged quantities of the variables. It is worth noting that $\boldsymbol{\mathcal{F}}_k^{\{1\}\downarrow} = \boldsymbol{F}_k^{\{1\}\downarrow-} = (rhu_n)_k^{\downarrow}$ represents the equilibrium bulk mass flux through out the intercell edge, i.e. without dilation contribution. Furthermore, the numerical method is able to deal with subcritical and supercritical wet-dry fronts, ensuring robust conservation for the solid and liquid phases and without requiring additional time step restrictions (Martínez-Aranda et al., 2020).

The stability of the explicitly computed numerical solution is addressed by the dynamical limitation of the global time step using a CFL condition (see Appendix C). The local time step allowed for each k edge is estimated here assuming that the absolute maximum of the eigenvalues $\widetilde{\lambda}_{m,k}$ corresponds to the fastest wave celerity. Hence the global time step Δt is limited by the minimum of the local time steps, i.e. the more restrictive instantaneous local flow features.

Finally, once the conservative variables have been updated to the next time $\mathbf{U}_i^{n+1}$ using (37), it is necessary to compute separately the flow depth h, bulk density ρ, depth-averaged velocity (u, v) along x- and y-coordinates and the solid concentration of each sediment class ϕ_p composing the fluidized material. The updated flow depth and bulk density of the fluidized material can be directly calculated as

$$\begin{aligned}h_i^{n+1}&=\mathbf{U}_i^{\{1\}n+1}-\mathbf{U}_i^{\{4\}n+1}\\ \rho_i^{n+1}&=\rho_w\,\frac{\mathbf{U}_i^{\{1\}n+1}}{h_i^{n+1}}\end{aligned} \tag{42}$$

being $\mathbf{U}_i^{\{\cdot\}n+1}$ the $\{\cdot\}$th component of the updated conservative variables vector at each cell $\mathbf{U}_i^{n+1}$. The velocity field is directly computed as

$$u_i^{n+1} = \frac{\mathbf{U}_i^{\{2\}n+1}}{\mathbf{U}_i^{\{1\}n+1}} \qquad v_i^{n+1} = \frac{\mathbf{U}_i^{\{3\}n+1}}{\mathbf{U}_i^{\{1\}n+1}} \tag{43}$$

4.2. Multi-grain solid phase updating

Furthermore, ensuring solid mass conservation in multi-grain water-sediment flows requires that the volume fraction of each pth sediment class, $(h\phi_p)_i$, must be updated separately as follows

$$(h\phi_p)_i^{n+1} = (h\phi_p)_i^n - \frac{\Delta t}{A_i}\sum_{k=1}^{\mathrm{NE}} (\mathcal{F}_{sp})_k^{\downarrow} l_k \tag{44}$$

where $(\mathcal{F}_{sp})_k^{\downarrow}$ is the upwind solid flux for the pth sediment class at the kth edge, computed as

$$(\mathcal{F}_{sp})_k^{\downarrow} = \left[(rhu_n)_k^{\downarrow} + \widetilde{\mathcal{L}}_{nk}\right]\left(\frac{\phi_p}{r}\right)_{\{upw\}}^n$$
$$\text{with}: \begin{cases} \{upw\} = i & \text{if} \quad (rhu_n)_k^{\downarrow} \geq 0 \\ \{upw\} = j & \text{if} \quad (rhu_n)_k^{\downarrow} < 0 \end{cases} \tag{45}$$

being $(rhu_n)_k^{\downarrow}$ the intercell bulk mass flux throughout the kth cell edge. Then the volumetric concentration of the pth sediment class in the flow column at the next time step $t = t^{n+1}$ is updated as

$$(\phi_p)_i^{n+1} = \frac{(h\phi_p)_i^{n+1}}{h_i^{n+1}} \tag{46}$$

It is worth noting that complex specific sediment-class processes, such as the bed material exchange, the sediment settling or the solid particle interactions, have been neglected in this work for the sake of simplicity. Nevertheless, these terms could be included easily for each sediment class as new source terms on the specific transport equation (44).

5. Numerical tests

5.1. Test A: One-dimensional dambreak over steep-bed of a frictional fluid

The aim of this synthetic test is to assess the influence of the shear-induced solid phase dilation on the flow dynamics. The one-dimensional dambreak of a pure-frictional fluidized mass over a dry steep 5% slope is simulated, being $h_0 = 30.5\,\mathrm{m}$ the initial depth of the fluidized material for $0 \leq x \leq 305\,\mathrm{m}$. This material consists of a mix of clear water and one sediment class with density $\rho_s = 2518\ \mathrm{kg/m^3}$ and initial volumetric concentration $\phi = 0.55$, leading to a uniform bulk density $\rho = 1835\ \mathrm{kg/m^3}$. The characteristic diameter of the solid particles is $d_s = 1\ \mathrm{mm}$ and the permeability of the solid aggregate is estimated as $\kappa = 10^{-8}\,\mathrm{m^2}$ (Iverson and George, 2014). The density and viscosity of the intergranular fluid are $\rho_w = 1000\ \mathrm{kg/m^3}$ and $\mu = 10^{-3}\,\mathrm{Pa\cdot s}$ respectively. Considering the dilatancy formula (9), the dilatancy constant is set to $k_1 = 0.1$ and the equilibrium solid concentration ϕ_{eq} is varied to enable three different initial dilation states, summarized as

Positive dilatancy:	$\phi_{eq} = 0.50$	$\tan\psi > 0$
Equilibrium state:	$\phi_{eq} = 0.55$	$\tan\psi = 0$
Negative dilatancy:	$\phi_{eq} = 0.60$	$\tan\psi < 0$

The basal resistance is here considered pure-frictional, hence $\tau_b = \tau_{fb} = (\rho g h - \mathcal{P}_b)\tan\delta_f$ (24) with the basal pore-pressure $\mathcal{P}_b = (1 + \mathcal{E}_b)\rho_w g h$, leading to

$$\tau_b = (r - 1 - \mathcal{E}_b)\rho_w g h \tan\delta_f \tag{47}$$

being $r = \rho/\rho_w$ the normalized bulk density and with a basal frictional stability angle $\delta_f = 6°$. The spatial domain is discretized using a 2D mesh width a single row of 10^4 square cells with $\Delta x = 0.5\,\mathrm{m}$, the final time simulated is $t = 100\,\mathrm{s}$ and the CFL is set to 1. Fig. 6 shows the temporal evolution of the flow free surface for the equilibrium state $\tan\psi = 0$ case.

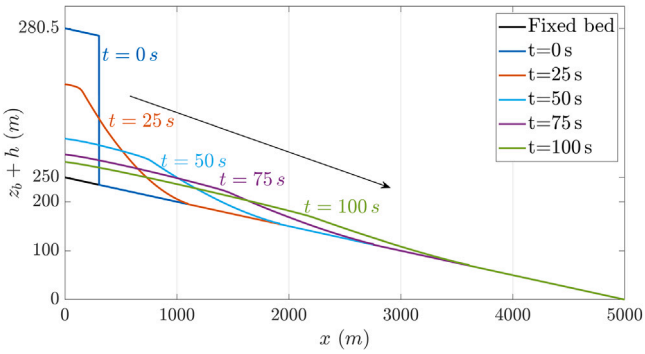

Fig. 6. Test A – Temporal evolution of the flow free surface for the equilibrium state $\tan\psi = 0$.

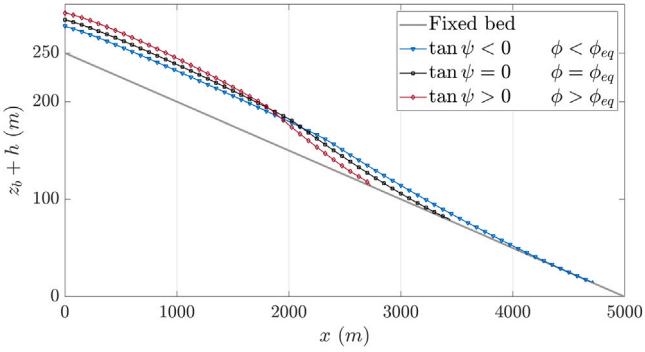

Fig. 7. Test A – Runout at $t = 100\,\mathrm{s}$ for positive dilatancy $\tan\psi > 0$, nil dilatancy $\tan\psi = 0$ and negative dilatancy $\tan\psi < 0$ states.

First, the effects of the solid-phase dilation over the flow mobility are assessed by neglecting the deviatoric term $\widetilde{\mathcal{L}}_{nk}$ (41) in the intercell solid flux (45), hence leading to a nil dilation flux contribution $\mathbf{L}_{\mathbf{n}k}^{\downarrow -} = 0$ (40). This implies that the solid concentration in the flow remains constant and uniform ($\phi = 0.55 = \mathrm{const}$), as it is seen below, demonstrating the well-balance behaviour of the model. Fig. 7 shows the runout distance of the flow at $t = 100\,\mathrm{s}$ for the three material states considered. For the equilibrium state, $\tan\psi = 0$, the pore pressure is hydrostatic and the frictional basal resistance reduces to $\tau_b^{Hst} = (\rho - \rho_w)gh\tan\delta_f$.

Positive dilatancy states, $\tan\psi > 0$, are related to a solid concentration larger than the equilibrium value ϕ_{eq}. Under this condition, the pore pressure is smaller than the hydrostatic, leading to a negative basal dynamic pore-pressure factor $\mathcal{E}_b < 0$ and increasing the frictional basal resistance $\tau_b > \tau_b^{Hst}$. Therefore, solid concentrations larger than the equilibrium value (dense packed mixtures) are associated to a lower flow mobility (see Fig. 7). Contrarily, negative dilatancy states ($\tan\psi > 0$) are associated to a solid concentration smaller than the equilibrium value and pore pressures larger than the hydrostatic. Hence, for these states, the basal pore pressure excess factor is positive $\mathcal{E}_b > 0$ and reduces the frictional basal resistance hence $\tau_b < \tau_b^{Hst}$. Therefore, loose packed mixtures (liquefied slurries) with concentrations lower than the equilibrium value are related to larger runout distances (see Fig. 7).

Second, the effects of the shear-induced dilation on the solid phase distribution within the flow is analysed. In this case, the frictional basal resistance is considered always hydrostatic $\tau_b = \tau_b^{Hst}$ in order to have similar runout distances regardless of the dilation state. Fig. 8 depicts the temporal evolution of the integrated dynamic pore-pressure $\mathcal{P}_e$ and the basal dynamic pore-pressure factor $\mathcal{E}_b$ for the positive dilatancy $\tan\psi > 0$ simulation. Note that the lowest integrated pore-pressure

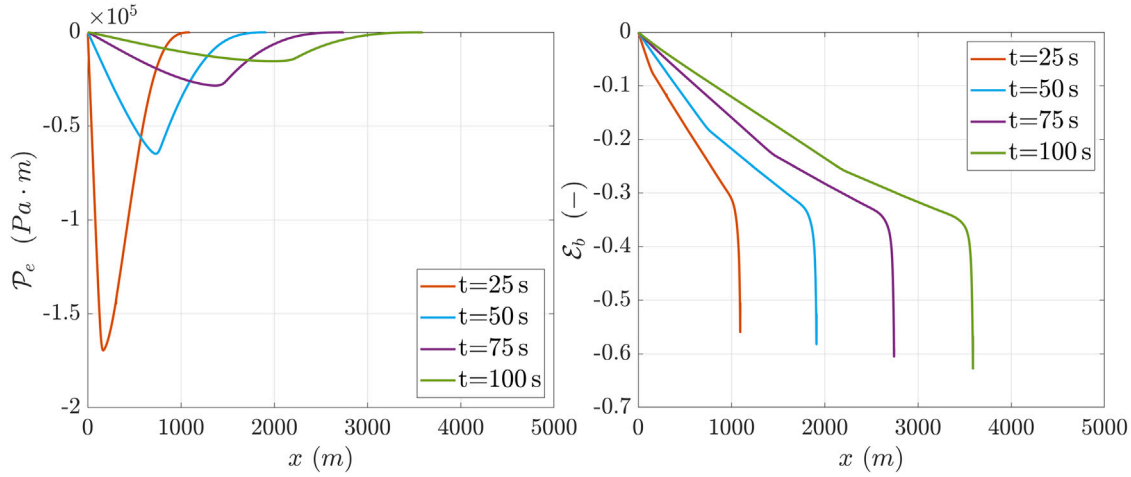

Fig. 8. Test A – Temporal evolution of (left) the integrated pore pressure excess $\mathcal{P}_e$ and (right) the basal pore pressure excess factor $\mathcal{E}_b$ for positive dilatancy $\tan\psi > 0$ states.

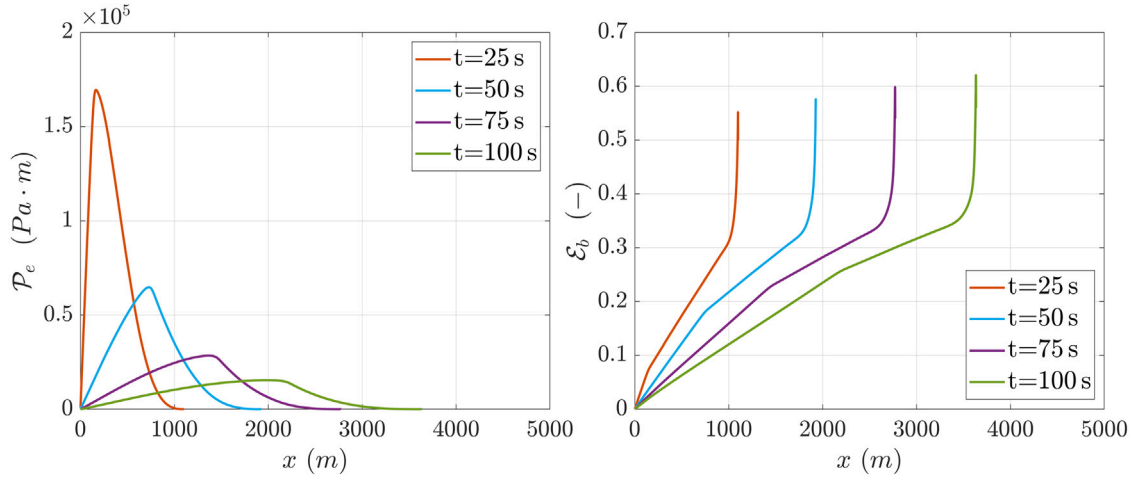

Fig. 9. Test A – Temporal evolution of (left) the integrated pore pressure excess $\mathcal{P}_e$ and (right) the basal pore pressure excess factor $\mathcal{E}_b$ for negative dilatancy $\tan\psi < 0$ states.

excess $\mathcal{P}_e$ corresponds to the centre region of the flow wave whereas the lowest basal pore pressure excess factor $\mathcal{E}_b$ are associated to the flow head and tail regions.

Conversely, when the solid aggregate undergoes negative dilation states with $\tan\psi < 0$ (see Fig. 9), the highest integrated dynamic pore pressure $\mathcal{P}_e$ appears at the centre region of the flow, but it is lower at the tail and head regions of the flow. The basal pore pressure excess factor $\mathcal{E}_b$ reaches its maximum at the wave front and decreases progressively along the centre and tail of the dambreak wave.

It is worth noting that, regardless of the dilation state, the integrated dynamic pore-pressure reaches its maximum values during the first stages of the dambreak flow and relaxes progressively with time as the flow moves downstream. Nevertheless, the basal dynamic pore-pressure factor $\mathcal{E}_b$ shows a more persistent behaviour but increases slightly as the flow moves downstream. The spatial distribution of the solid phase within the dambreak wave is a consequence of the balance between the gradient of the integrated dynamic pore-pressure $\frac{\partial \mathcal{P}_e}{\partial x}$ and the contribution of the basal pressure excess $\mathcal{E}_b \rho_w g h \frac{\partial z_b}{\partial x}$, resulting in the deviatoric dilation-related contribution to the solid flux $\widetilde{\mathcal{L}}_{nk}$ (41). Fig. 10 shows the solid phase distribution at $t = 100\,\mathrm{s}$ along the dambreak wave for the positive dilation, negative dilation and equilibrium states.

For the equilibrium state, $\tan\psi = 0$, the pore pressure is hydrostatic and the solid particles move with the mixture velocity. There do not exist differences between the solid and liquid phases and hence the solid concentration remains constant, maintaining the initial uniform value. When positive or negative dilation occur, pore pressure gradients appear within the flow and hence the solid particles move with a velocity different from the liquid phase velocity. Generally, the pore-fluid flows from high pressure to low pressure zones. Therefore, the sediment fraction in low pore pressure regions ($\phi \gg \phi_{eq}$) undergoes a porosity creation process, decreasing the solid concentration in those regions. Contrarily, high pressure regions ($\phi \ll \phi_{eq}$) suffer an outlet liquid flow and the solid phase undergoes a contraction process, hence increasing its concentration. Both dilation states lead to the bulk solid concentration ϕ converging to the equilibrium value ϕ_{eq} with time.

This simple reasoning explains the solid distribution shown in Fig. 10, taking into account that this benchmark case is designed for enhancing the dependence of the solid phase dilation on the gradients of the integrated pore pressure $\mathcal{P}_e$, following Eqs. (28)–(29). On the one hand, for positive dilation states ($\phi > \phi_{eq}$ and $\tan\psi > 0$), the lowest values of the integrated pore pressure $\mathcal{P}_e$ appear at the centre region of the wave (see Fig. 8) and cause the pore-fluid to migrate from the head to the centre region. Therefore, the solid concentration at the centre region slightly decreases ($\phi \to \phi_{eq}$), whereas the solid concentration at the head undergoes a marked increase. Note that the slight decrease on the solid concentration at the centre of the wave is balanced by a high increment of the solid concentration in the head region due to the lower flow depths at the wave front. This behaviour is a direct consequence of the fully conservative character of the numerical method for the solid and liquid phases. On the other hand, for negative dilation states ($\phi < \phi_{eq}$ and $\tan\psi < 0$), the centre region of the wave shows a

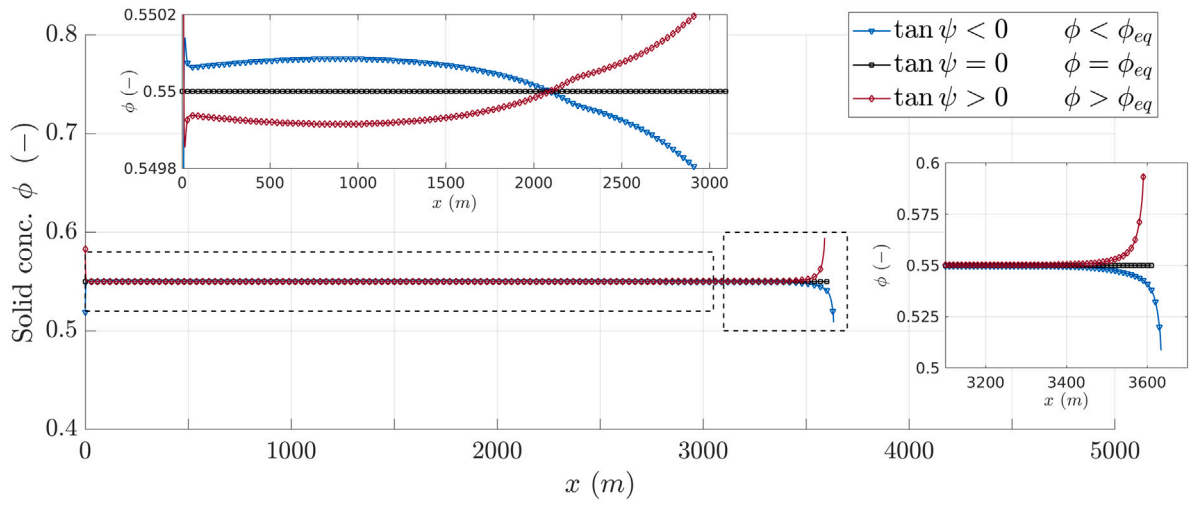

Fig. 10. Test A – Spatial distribution of the solid concentration at $t = 100$ s for positive dilatancy $\tan\psi > 0$, equilibrium $\tan\psi = 0$ and negative dilatancy $\tan\psi < 0$ states.

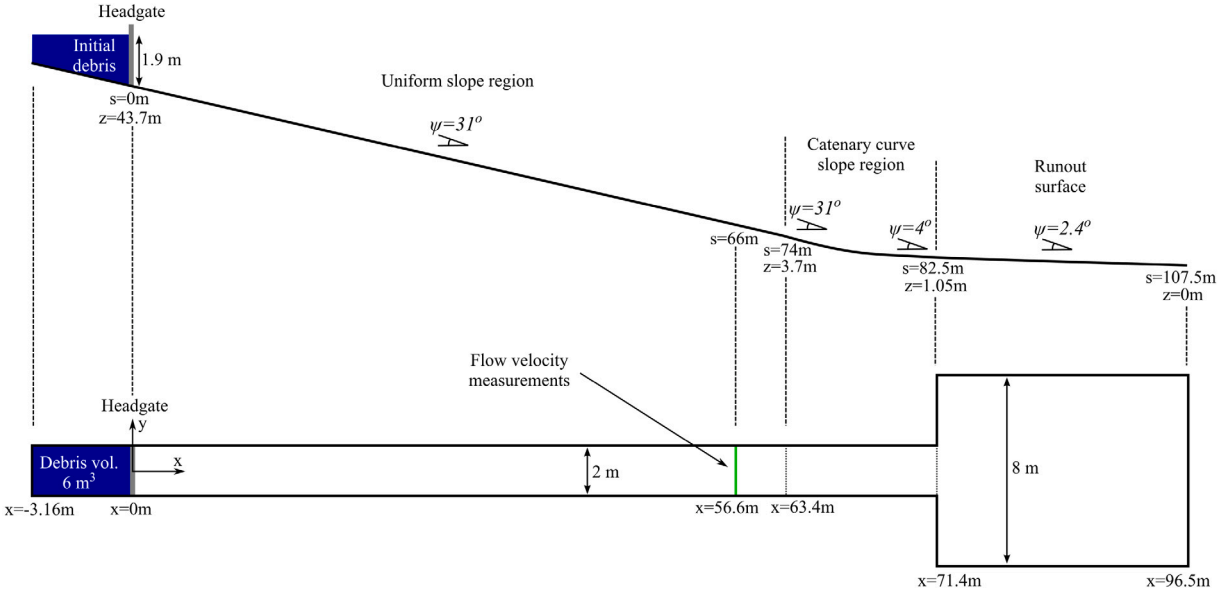

Fig. 11. Test B – Sketch of the USGS debris dambreak experiments.

higher integrated pore pressure $\mathcal{P}_e$ than the wave head (see Fig. 9). This creates a pore-fluid outflow from the centre region to the wave head. Consequently, the solid concentration slightly increases at the centre zone ($\phi \to \phi_{eq}$), whereas it shows a remarkable decrease at the head because of the lower flow depths at the wave front.

5.2. Test B: USGS debris dambreak over rigid steep bed

In this benchmark case, the proposed density-variable model including the effects of the shear-induced solid phase dilation is validated using data from large-scale experiments consisting of dambreak debris flows over a steep fixed bed. The experiment was carried out in the USGS large-scale debris-flow flume and data from two repetitions, called run I (date 12/9/2006) and J (date 19/6/2007), were reported by Iverson et al. (2011). The USGS debris-flow flume is a straight rectangular concrete channel 95 m long, 2 m wide and 1.2 m deep with a vertical headgate placed 12.5 m downstream the channel beginning, which retains the static debris material until the experiment initial time. Fig. 11 shows a schematic representation of the USGS debris-flow flume for these fixed-bed experiments. All the longitudinal distances s taken along the experimental flume floor are referred to the headgate position. The channel had an 31° uniform slope until $s = 74$ m, where the flume began to flatten following a catenary curve and evolving to a 4° slope at $s = 82.5$ m. Then, the flume debouched onto a 15 m long, 8 m wide and 2.4° slope concrete runout surface.

The initial features of the debris aggregate were previously reported in Iverson et al. (2010). The initial debris volume was 6 m^3, composed by a fully saturated mixture of water and gravel, sand and mud grains with 60% bulk solid concentration. For the sake of simplicity, a unique bulk sediment class is considered here, with an equivalent characteristic diameter $d_s = 6.9$ mm and solid density $\rho_s = 2700$ kg/m^3, leading to an initially uniform bulk density $\rho = 2020$ kg/m^3. Table 1 shows the main parameters used in the simulations for characterizing the debris mixture. The pore-fluid is considered clear water ($\rho_w = 1000$ kg/m^3 and $\mu = 0.001$ Pa · s) and the uniform solid-aggregate permeability is set to $\kappa = 10^{-8}$ m^2 (Iverson and George, 2014). In order to reduce the number of setup parameters involved in the simulations, a constant shearing-equilibrium concentration $\phi_{eq} = 0.65$ is considered. This value is slightly higher than the actual initial solid concentration, since an extra water amount was added to the debris mixture before the experiment beginning, but lower than the lithostatic deposition concentration

Table 1
Test B – Characteristic values used for the simulation setup.

Debris volume	6 m^3
Initial solid concentration ϕ_0	0.60
Debris water content	40%
Bulk debris density ρ	2020 kg/m^3
Solid particles diameter d_s	6.9 mm
Solid density ρ_s	2700 kg/m^3
Shearing-equilibrium concentration ϕ_{eq}	0.65
Pore-fluid density ρ_w	1000 kg/m^3
Pore-fluid viscosity μ	0.001 Pa · s
Porous media permeability κ	10^{-8} m^2

Table 2
Test B – Characteristic of the computational meshes used for the convergence analysis and final runout distance.

Mesh	Cell area	Number of cells	Comp. time	Runout distance
Mesh 1	800 cm^2	7132	2.23 s	82, 71 m
Mesh 2	400 cm^2	14259	3.50 s	82, 61 m
Mesh 3	200 cm^2	28388	5.12 s	82, 56 m
Mesh 4	100 cm^2	57212	12.01 s	82, 56 m

$\phi_{max} = 0.73$ estimated with the Wu (2007) empirical relation for deposit porosity.

In the experiments, once the headgate was opened, the debris dambreak wave accelerated over the uniform-slope rigid bed region of the flume until it reached the catenary-slope zone and the runout surface where it stopped. For each run of the experiment, Iverson et al. (2011) tracked the wave-front location during the flow advance using image techniques and video frames. The wave-front velocity was also measured between $s = 60$ m and $s = 70$ m from the video frames, as well as the final runout distance after flow detention. Moreover, video files of both experiments are available in https://pubs.usgs.gov/of/2007/1315/.

The simulations are performed using an unstructured triangular mesh, with CFL = 0.95, for a simulated time (25 s) enough to ensure full detention at the runout surface. Following Li et al. (2018), the basal resistance is modelled using the frictional–turbulent closure (23), setting a frictional stability angle for the solid phase $\delta_f = 40°$ and a Manning's roughness parameter $n_b = 0.018\,\mathrm{sm}^{-1/3}$ for the rigid flume bed. Note that these values for the resistance estimation have not been calibrated but directly taken from the original experimental data (Iverson et al., 2010). First, a mesh convergence analysis is carried out, setting the dilatancy tuning parameter $k_1 = 0$ (i.e. $\tan\psi = 0$) and decreasing the averaged area of the computational cells from 800 cm^2 to 100 cm^2 progressively. Table 2 summarizes the characteristics of the computational meshes, the computational effort required to perform each simulation and the final runout distance predicted. Furthermore, Fig. 12 depicts the flow depth profile along the steep channel at different times for all the meshes used in the convergence analysis. Both the flow evolution as the wave progresses downstream and the final runout distance show low dependence on the mesh refinement. Also, the model performance is almost 12 times faster-than-real-time (FTRT) for the most coarse mesh and 2 times FTRT for the finest mesh. From now on, the rest of simulations are performed using Mesh 3, with $A = 200$ cm^2 and almost 28400 triangular cells.

In order to analyse the influence of the shear-induced dynamic pore-pressure on the flow mobility, the dilatancy $\tan\psi$ of the solid phase is controlled by varying the tuning parameter k_1 in the range $0 \leq k_1 \leq 0.15$ (9). It is worth highlighting that k_1 should be calibrated for each case depending on the specific features of the water-solid mixture. Fig. 13 shows the depth of the debris deposit after the flow detention ($t = 25$ s). Note that the distances are expressed in the horizontal x-coordinate. The red rectangle at $x \approx 82$ m ($s \approx 93$ m) indicates the wave front detention in the experimental runs. After the flow initialization,

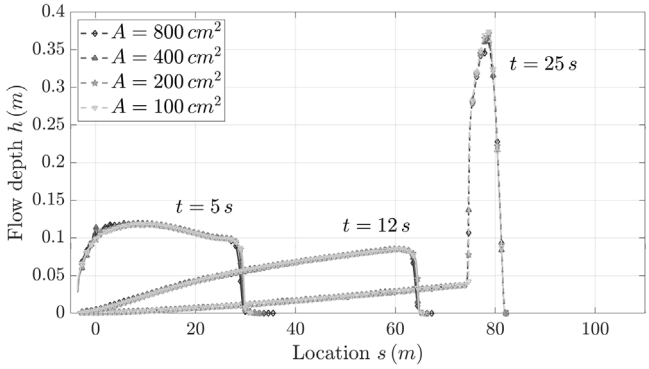

Fig. 12. Test B – Deposit depth h after the flow detention ($t = 25$ s) with Mesh 1 ($A = 800$ cm^2), Mesh 2 ($A = 400$ cm^2), Mesh 3 ($A = 200$ cm^2) and Mesh 4 ($A = 100$ cm^2).

the dambreak wave progresses downslope rapidly until it reaches the runout surface, where it stops.

Analysing the model behaviour, the debris material undergoes increasing shearing states as it accelerates over the steep slope. These shearing states are associated to positive pore pressures throughout the flow column, since the solid phase is initially under a negative dilatancy state $\tan\psi < 0$. This dynamic pore-pressure modifies the basal resistance against the movement and induces the separation of the solid and liquid phases. As the tuning parameter k_1 is increased from the equilibrium state $k_1 = 0$ to the maximum dilation considered ($k_1 = 0.15$), the mobility of the debris flow grows and leads to larger runout distances. This enhanced mobility is explained by the reduction of the frictional yield strength as the basal value of the positive dynamic pore-pressure increases.

Fig. 14 shows the basal dynamic pore-pressure factor $\mathcal{E}_b$ records as the dambreak wave passes the probe section $x = 56.6$ m ($s = 66$ m). First, the recorded values of $\mathcal{E}_b$ increase as the parameter k_1 grows, i.e. as the dilatancy $\tan\psi$ increases. However, the relation between the shear-induced basal dynamic pore pressure and the hydrostatic basal pore pressure (only related to the flow depth h) is clearly non-linear and non-monotonic, showing a relative hysteresis phenomenon regardless of the value of the dilatancy parameter $k_1 > 0$ considered.

Therefore, as the dilatancy tuning parameter k_1 is increased, the positive basal pore pressure excess factor $\mathcal{E}_b$ also increases for equal values of flow density, depth and velocity, reducing the effective normal stress σ_e at the bed-flow interface. This reduction of the effective normal stress leads directly to the reduction of the basal frictional yield strength τ_f and hence to lower basal resistance stresses against the dambreak wave advance over the steep flume. Fig. 15–(a) depicts the numerical wave-front location along the experimental channel as time progresses, compared with experimental data. As the dilatancy tuning parameter k_1 is increased, the acceleration of the front advance along the uniform-slope region of the flume also increases. Hence, the numerical wave-front location tends to adapt to the observed data when the shear-induced pore pressure is enhanced. Nevertheless, marked differences with the laboratory data appear along the runout region, probably due to the self-consolidation process of the fluidized material, which is not considered in the model.

The velocity of the dambreak advance is clearly observed in Fig. 15–(b), where the numerical wave-front velocity has been depicted against the experimental data. Iverson et al. (2011) reported a unique front velocity value at 60 m < s < 70 m of 12.5 m/s for the experimental run I and 7.1 m/s for the experimental run J (grey rectangle) but the velocity evolution can be derived from the experimental front location data. Increasing the dilation state of the solid phase, i.e. increasing k_1, leads to a better prediction of the wave-front velocity compared with those of the equilibrium state ($\tan\psi = 0$) simulation. Note that for $k_1 \in [0.10, 0.15]$ the computed front velocity agrees with the experimental

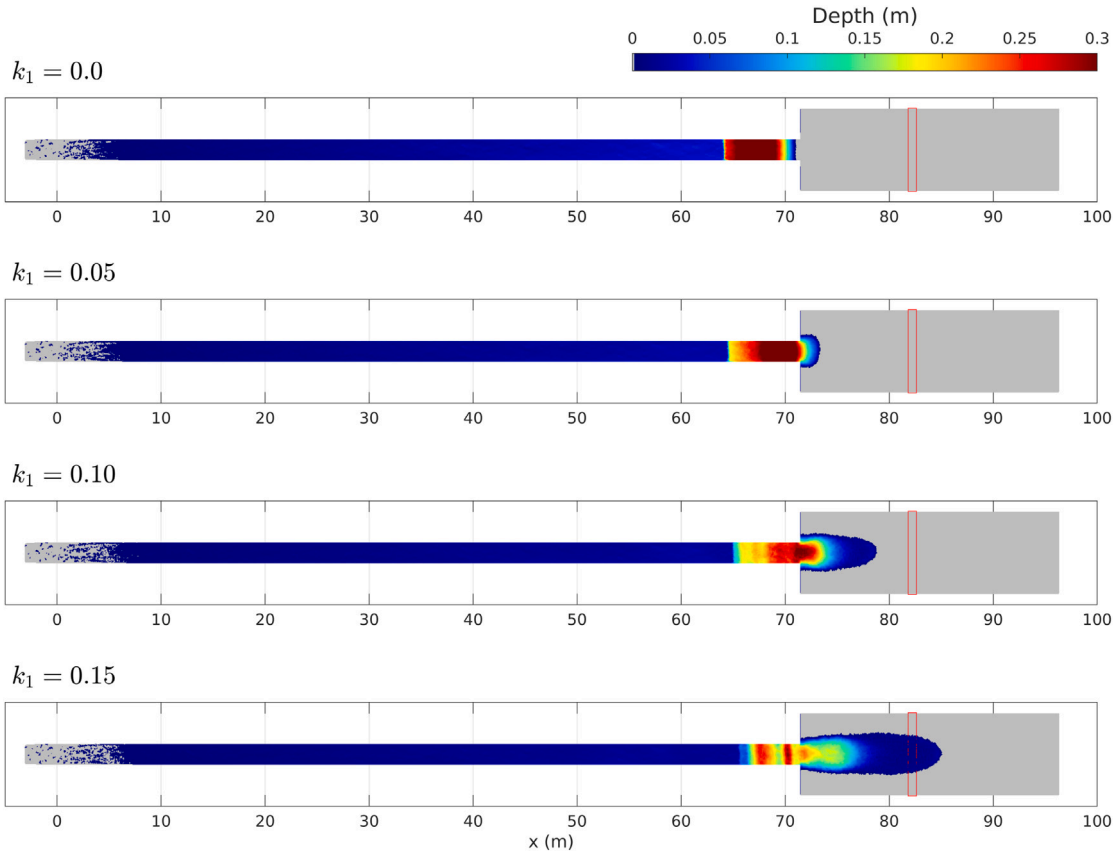

Fig. 13. Test B – 2D deposit depth h after the flow detention ($t = 25$ s) with values of the dilatancy tuning parameter $k_1 = 0$ (equilibrium), $k_1 = 0.05$, $k_1 = 0.10$ and $k_1 = 0.15$ (maximum dilation).

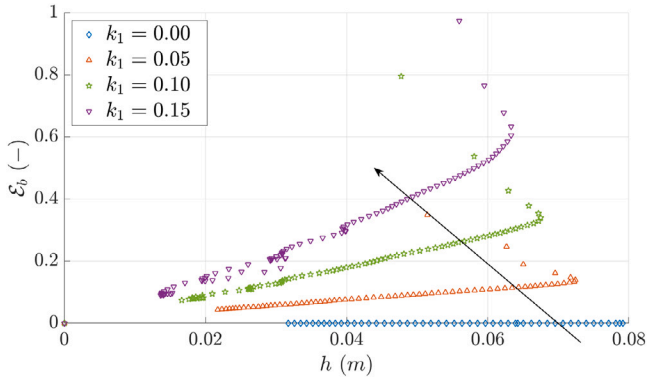

Fig. 14. Test B – Basal dynamic pore-pressure factor $\mathcal{E}_b$ at the probe section $x = 56.6$ m ($s = 66$ m) with values of the dilatancy tuning parameter $k_1 = 0$ (equilibrium), $k_1 = 0.05$, $k_1 = 0.10$ and $k_1 = 0.15$ (maximum dilation).

data all over the dambreak progression along the constrained channel but differences arise for the flow detention at the catenary and runout zones.

Fig. 16 shows the depth-averaged density distribution after the flow detention at $t = 25$ s. As the dilatancy tuning parameter k_1 is increased, the positive pore pressure excess also increases and leads to the separation of the solid and liquid phases throughout the dambreak wave. In the numerical simulations, as the dambreak progresses along the constrained channel ($s < 82.5$ m), a liquefied wave-head is predicted with a lower solid concentration and high dynamic pore-pressure which enhances the debris mobility. Once the main dambreak wave reaches the runout surface, the velocity decreases and the induced pore pressure

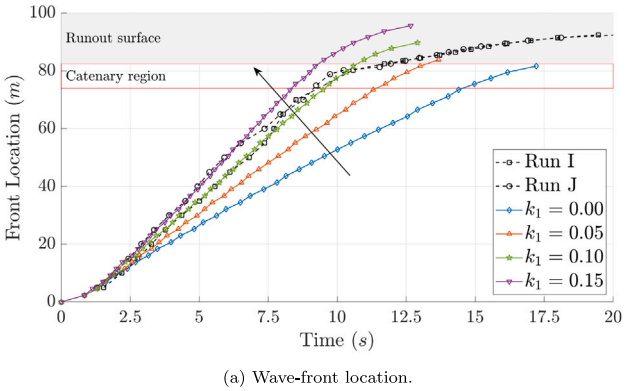

(a) Wave-front location.

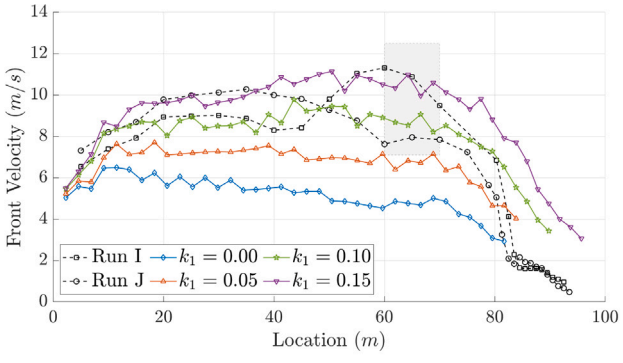

(b) Wave-front velocity.

Fig. 15. Test B – Temporal evolution of the dambreak wave-front: (a) Time vs. Location and (b) Location vs. Velocity.

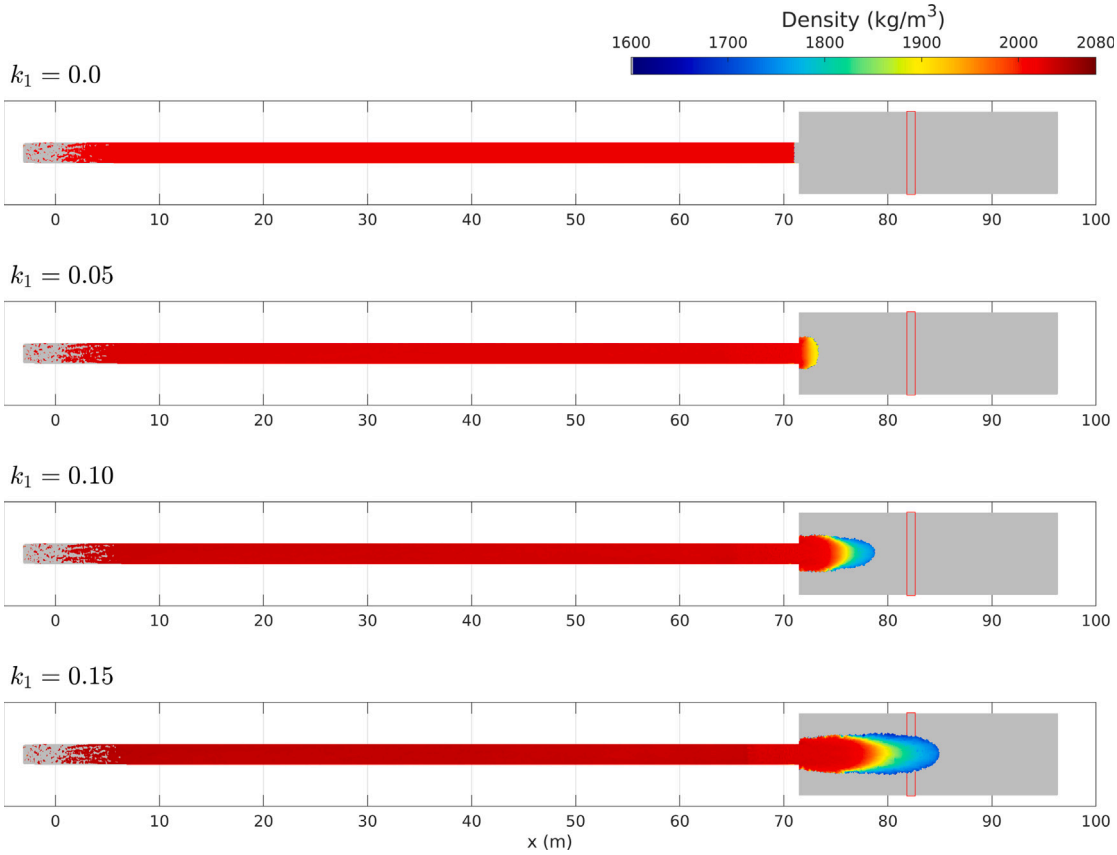

Fig. 16. Test B – 2D deposit density h after the flow detention ($t = 25$ s) with values of the dilatancy tuning parameter $k_1 = 0$ (equilibrium), $k_1 = 0.05$, $k_1 = 0.10$ and $k_1 = 0.15$ (maximum dilation).

excess dissipates at the flow head, increasing the frictional stresses in the solid phase and stemming the wave-front finally. This liquefied head becomes more marked as the dilatancy tuning parameter k_1 is increased and can be observed in the video recording of the experiments.

Nevertheless, although the main wave is stopped at the runout surface, the movement of the material at the steep slope region continues generating rolling waves which reach progressively the detention zone. Fig. 17 shows the cross-section averaged value of the basal pore pressure excess factor $\mathcal{E}_b$ at times $t = 6,\ 12,\ 15$ and 18 s for the simulation with dilatancy tuning parameter $k_1 = 0.15$. The fully-liquefied flow head is observed for $t = 6$ s whereas the main wave detention occurs at $t = 12$ s approximately. Secondary rolling waves associated to increments of the shear-induced basal pore pressure are developed for $12 \leq t \leq 22$ along the steep slope and stop at the catenary region and at the beginning of the runout surface, increasing the final deposit head in these regions. These secondary rolling waves behind the main flow front can also be observed in the video recording of the experiments. This behaviour is known as surge dynamics and is one of the mean features of the debris flows, mainly associated to the appearance of non-uniform shear stresses along the debris flow.

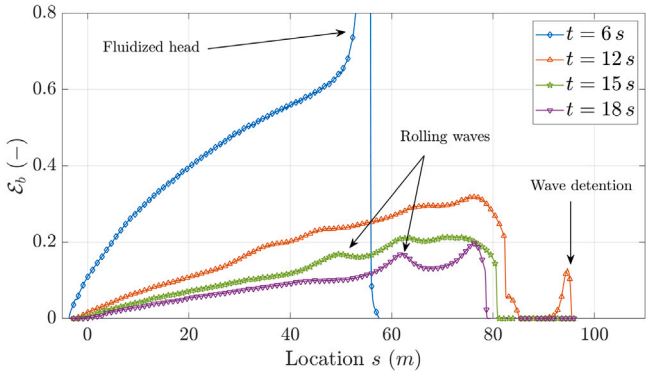

Fig. 17. Test B – Longitudinal profile of the basal pore pressure excess factor $\mathcal{E}_b$ at times $t = 6,\ 12,\ 15$ and 18 s for the simulation with dilatancy tuning parameter $k_1 = 0.15$.

5.3. Test C: Mine tailings dam failure in Brumadinho

We assess in this section the performance of the shear-induced dilation model for simulating a real large-scale and highly unsteady mud flow, including multiple sediment classes composing the fluidized material. The real event occurred on January 25th, 2019, at 9 km North-East of Brumadinho city (Minas Gerais, Brazil). A mine dam containing iron waste tailings suffered a sudden catastrophic failure, causing an extremely rapid mud flow which travelled downstream more than 10 km. This catastrophic event caused more than 260 deaths, as well as massive environmental and economic losses. The mining tailings inside the dam were $12 \cdot 10^6$ m^3 approximately, with a height of almost 80 m near the contention dyke and covering a terrain area of $4.2 \cdot 10^5$ m^2. The structural collapse of contention dike was complete in less than 10 seconds and most of the mine tailings became a fluidized material which flowed out the dam during the first 5 minutes after the dike collapse. This material, highly loaded with heavy metal particles, progressed downstream and created a high-speed large-height mud wave which travelled 8.5 km downstream in less than 45 minutes, reaching the Paraopeba River (see Fig. 18).

Tailings consisted of water, mineral sand (38%) and fine solids (62%), including mineral silt-clay and heavy metals particles. Before the dam collapse, the water content in the tailings material

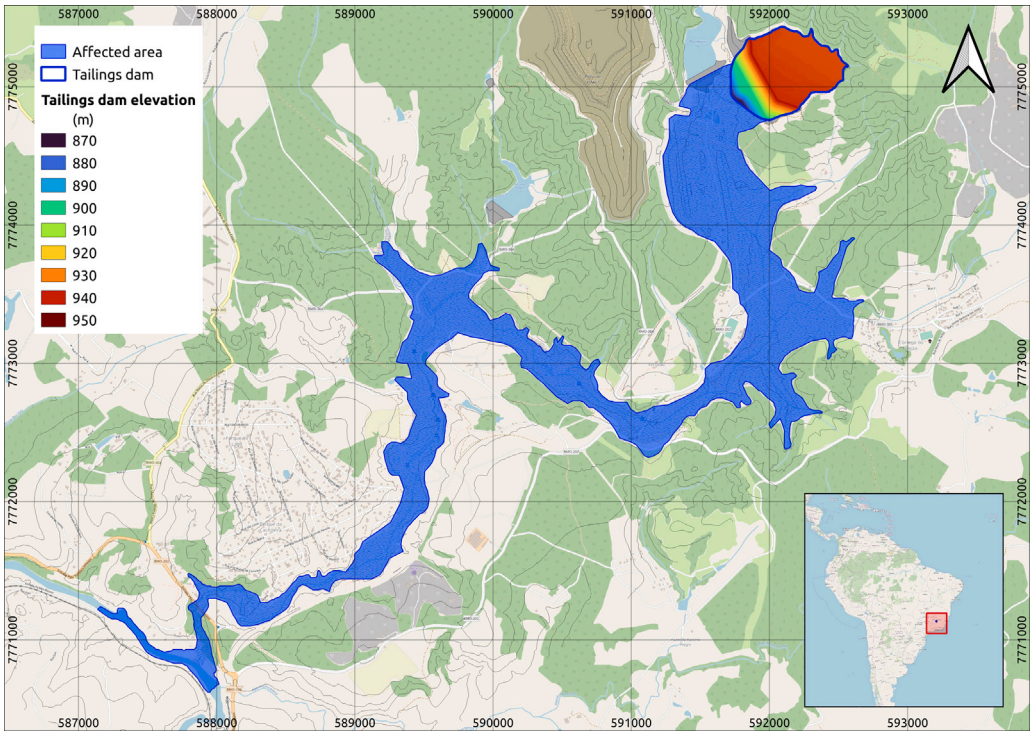

Fig. 18. Test C – Map of the area affected by the mud wave after the dam failure. The mine tailings dam is at the north east and the Paraopeba river is located at the south west.

was estimated around 50% by volume, with $24\,\mathrm{kN/m^3}$ bulk specific weight (Robertson et al., 2019). For these simulations, six different solid classes (mineral sand, mineral silt, iron, aluminium, manganese and titanium) are considered, satisfying the initial condition for the bulk solid concentration $\phi = \sum_{p=1}^{NS} \phi_p = 0.5$. The permeability of the solid aggregate was estimated as $\kappa = 10^{-8}\,\mathrm{m^2}$, the equilibrium lithostatic concentration was set to $\phi_{eq} = 0.65$ and a dilatancy tuning parameter $k_1 = 0.5$ was considered. The effective friction angle for the basal frictional shear stress was set to $\delta_f = 5°$, whereas a uniform Manning roughness parameter $n_b = 0.065\,\mathrm{ms^{-1/3}}$ was estimated since the previous land use downstream the dam was mainly forest and agriculture. A spatial domain of almost $12\,\mathrm{km^2}$ was discretized using an unstructured mesh with almost 0.6 millions triangular cells, refined at the near-dam region. The duration of the simulated event was 3 hours and the model performance ranged between 15 and 8 times FTRT, depending on the selected dilation parameters.

First, the sensitivity of the model to the basal pore-pressure was tested in terms of flow mobility. For the sake of simplicity, the dilation of the solid phase was neglected in this set of simulations but a uniform/constant value for the basal dynamic pore-pressure factor $\mathcal{E}_b$ was set manually. The value of $\mathcal{E}_b$ was increased gradually from $\mathcal{E}_b = 0.9$ (reduced pore-pressure effect on the basal resistance) to $\mathcal{E}_b \to \infty$ corresponding to a fully-liquefied mixture which undergoes null frictional shear stresses. Fig. 19 shows the location of the wave-front downstream the dam as time progresses. The grey rectangle indicates the observed time required by the mud wave to reach the Paraopeba river $8.5\,\mathrm{km}$ downstream the dam. As the value of $\mathcal{E}_b$ is increased, the basal resistance term is reduced and the flow mobility is boosted. A uniform/constant $\mathcal{E}_b = 1.05$ is required to achieve the same arriving time interval to the Paraopeba River as it was observed during the real event (32-47 min). For larger values of $\mathcal{E}_b$ the fluidized material shows even larger mobility, with an arrival time of 28 min for the fully-liquefied case (dashed line).

Then, the dilation of the solid phase is included in a second set of simulations, computing its effects on both the shear-induced pore-pressure and the basal resistance. This second set of simulations aims

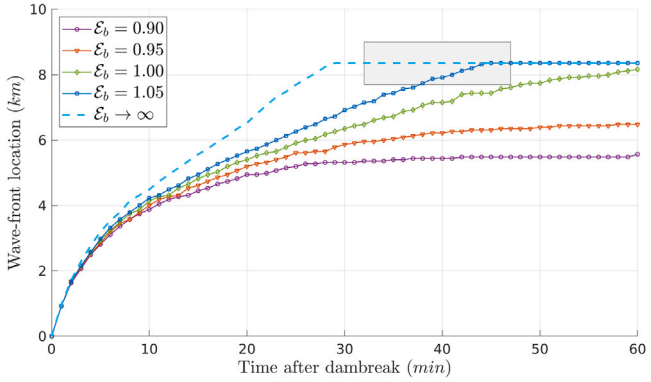

Fig. 19. Test C – Runout distance of the mud wave neglecting solid dilation and depending on the (constant) basal dynamic pore-pressure factor $\mathcal{E}_b$.

to test the sensitivity of the model to the intergranular fluid viscosity. Fig. 20 shows the runout distance of the flow as time progresses for different values of the pore-fluid viscosity between $\mu = 0.001\,\mathrm{Pa \cdot s}$ (clear water) and $\mu = 0.0025\,\mathrm{Pa \cdot s}$ (low-plasticity muddy slurry). A higher intergranular fluid viscosity leads to the development of larger shear-induced dynamic pressures, reducing the frictional shear stress between solid grains and hence increasing the mobility of the flow. Considering a viscosity value twice the clear water viscosity, i.e. $\mu = 0.002\,\mathrm{Pa \cdot s}$, allows to predict the observed arrival time of the mud wave to the Paraopeba river (32–47 min). However, in this case, the wave-front advance along the valley thalweg is not as gradual as in the above case with uniform/constant $\mathcal{E}_b$ and several "stop & go" events can be observed in the numerical results. These "stop & go" events are mainly caused by the coupling of the shearing state and the dynamic pore pressure when the shear-induced dilation of the solid aggregate is considered. The arrival of secondary waves to the wave-front zone, which is almost stopped, causes the appearance of dynamic pore pressures and the reduction of the frictional shear stress between

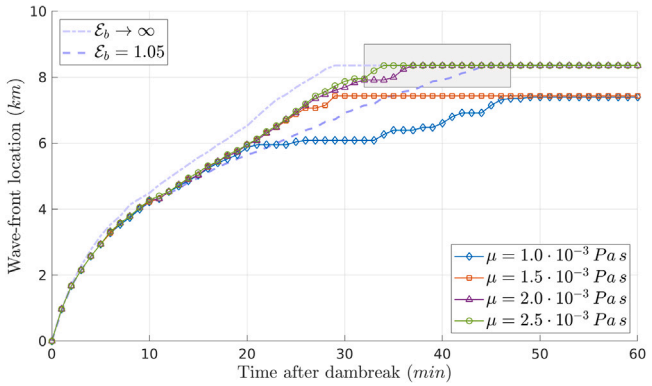

Fig. 20. Test C – Effects of the intergranular fluid viscosity on the runout distance of the mud wave including solid dilation.

sediment grains, leading to the reactivation of the whole fluidized material at the wave-front.

Fig. 21 shows the evolution of the mud wave for the case $\mu = 0.002\,\mathrm{Pa}\cdot\mathrm{s}$ at 5, 15, 30 and 45 minutes after the dam failure. The left column shows the depth-averaged flow velocity, which can be larger than 10 m/s in some regions, especially at the first stages after the dam failure. Note that, if a uniform/constant value of the basal dynamic pore pressure factor $\mathcal{E}_b$ is set and the dilatancy effects are neglected, the front celerity decreases progressively as the wave moves downstream (see Fig. 19). The pure Newtonian turbulent behaviour is here indicated by the curve $\mathcal{E}_b \to \infty$ and, as $\mathcal{E}_b$ decreases, the frictional shear stress grows and boosts the velocity reduction. Nevertheless, if the shear-induced dilation of the solid phase is included into the model (see Fig. 20), the flow mobility can be maintained at longer distances and larger durations since the dynamic pressure in the intergranular fluid is enhanced even far way downstream the initial dam location. These persistent dynamic pressures in the pore-fluid have been observed in real debris flow phenomena (McArdell et al., 2007). Focusing on the flow behaviour at the region close the confluence with the Paraopeba river (8.5 km downstream the dam), first the mud wave front almost stops at $t \approx 30\,\mathrm{min}$, but then it reactivates and increases its velocity suddenly at $t \approx 45\,\mathrm{min}$.

The right column in Fig. 21 shows the spatial distribution of the basal dynamic pore-pressure factor $\mathcal{E}_b$ at 5, 15, 30 and 45 minutes after the dam failure. At zones with nil velocity, the pore-pressure is purely hydrostatic, leading to lithostatic stresses in the flow column and causing the basal pore-pressure factor $\mathcal{E}_b = 0$. Nevertheless, at zones where the flow velocity is high, the fluidized material undergoes large shear rates and important dynamic pore pressures, leading to high values of the basal pore-pressure factor $\mathcal{E}_b$. At the first stages after the dam failure, high values of the basal dynamic pore-pressure factor are computed for the head, centre and tail regions of the mud flow. However, as the wave progresses downstream, the basal pore-pressure at the head region of the mud wave starts to reduce, causing higher frictional stresses and lower mobility (see $\mathcal{E}_b$ distribution 30 and 45 minutes after the dam failure). Contrarily, the basal pore-pressure factor $\mathcal{E}_b$ at the wave centre/tail region remains high even 45 minutes after the dam failure. In these regions, the material is fully-liquefied during most of the mud wave movement and the basal resistance associated to the frictional stress in the solid aggregate is almost null, leading to a high flow mobility.

Furthermore, the dilation of the solid aggregate causes not only the appearance of dynamic pore-pressured but also the separation of the solid and liquid phases as the mud wave moves downstream. The left column in Fig. 22 shows the computed height of the mud wave for the case $\mu = 0.002\,\mathrm{Pa}\cdot\mathrm{s}$ at 5, 15, 30 and 45 minutes after the dam failure. The total area that was affected by the mud wave has also been plotted here for comparison (green polygon). The depth of the mud flow can be up to 16 m in some zones, even far way downstream the dam location, indicating the destructive energy of this event. The agreement between the observed affected area and the numerical results at the arrival time $t = 45\,\mathrm{min}$ can be highlighted.

Finally, Fig. 22-right depicts computed spatial distribution of the bulk solid phase concentration ϕ at the same times after the dam failure. Initially, the solid concentration in the tailings inside the dam is uniform, i.e. $\phi = 0.50$, but a liquefied front appears in the mud wave once the flow starts, with a bulk solid concentration around $\phi \approx 0.40$ (see $t = 5\,\mathrm{min}$). Then, as the mud wave moves downstream, the solid material accumulates progressively at the wave-front due to the dynamic pressure gradients within the intergranular fluid induced by shearing of the solid aggregate. A highly concentrated front appears as the mud wave progresses, with $\phi \approx 0.70$, leading to lower basal pore-pressures and hence increasing the frictional resistance at the wave-front (see $t = 30\,\mathrm{min}$ and $t = 45\,\mathrm{min}$). Contrarily, the solid concentration at the wave-tail evolves to lower values, with $\phi \approx 0.45$–0.50, indicating also a more liquefied behaviour (lower basal resistance) of the flow at this zone. This separation process of the solid material from the liquid phase has usually been observed in real mud/debris flows (Jakob and Hungr, 2005) but it cannot be achieved by the classical quasi-single phase models, which should compute constant solid concentrations in this case.

6. Conclusions

This work is concerned with the mathematical and numerical modelling of densely packed water-sediment surface flows, such as mud and debris flows, where the fluidized material is composed by a heterogeneous mix of water and multiple solid phases, which moves rapidly over complex steep topographies. These physical features increase the complexity of the mathematical modelling for these kind of surface flows. Among all this complexity, probably the most challenging and unknown process is the development and persistence of high pressures within the intergranular fluid filling the pores. When the solid particles are transported throughout the entire flow column, the liquid and solid phases might have different velocities and hence might lead to the separation of the solid and liquid phases and the development of dynamic pressures in the pore-fluid. In this paper, for the first time from the authors knowledge, a closure relation for the shear-induced intergranular fluid pressure distribution during the movement of densely packed solid–liquid mixtures has been obtained and analysed. This pore pressure affects the effective normal stress along the flow column, leading to a modification of the frictional shear stress between solid particles respect to the hydrostatic condition and changing the basal resistance, hence affecting the flow mobility. Moreover, using this new pore pressure distribution, the effects of the sediment particles dilation have been included into the depth-averaged solid transport equation, leading to a novel formulation for the advective solid fluxes which includes the shear-induced separation of the solid aggregate from the pore liquid phase.

The resulting 2D shallow-type system of equations for contractive/dilative multi-grain water-sediment flows have been solved using a Finite Volume (FV) method, supplemented with the upwind resolution of the intercell fluxes using a fully-coupled augmented-Roe solver. The proposed method ensures the robust and accurate computation of the intercell fluxes for any type of steady and transient flow regime, even involving highly transient density interfaces, as well as the well-balanced behaviour of the solution in quiescent and steady states. The effects of the shear-induced solid phase dilation on the pore-fluid pressure have been also included into the intercell solid flux by a deviatoric contribution. Two important differences arise here in comparison with the classical quasi-single-phase approach: first, the separation of the solid aggregate from the pore-fluid movement within the flow is caused by a shear-induced deviatoric contribution to the

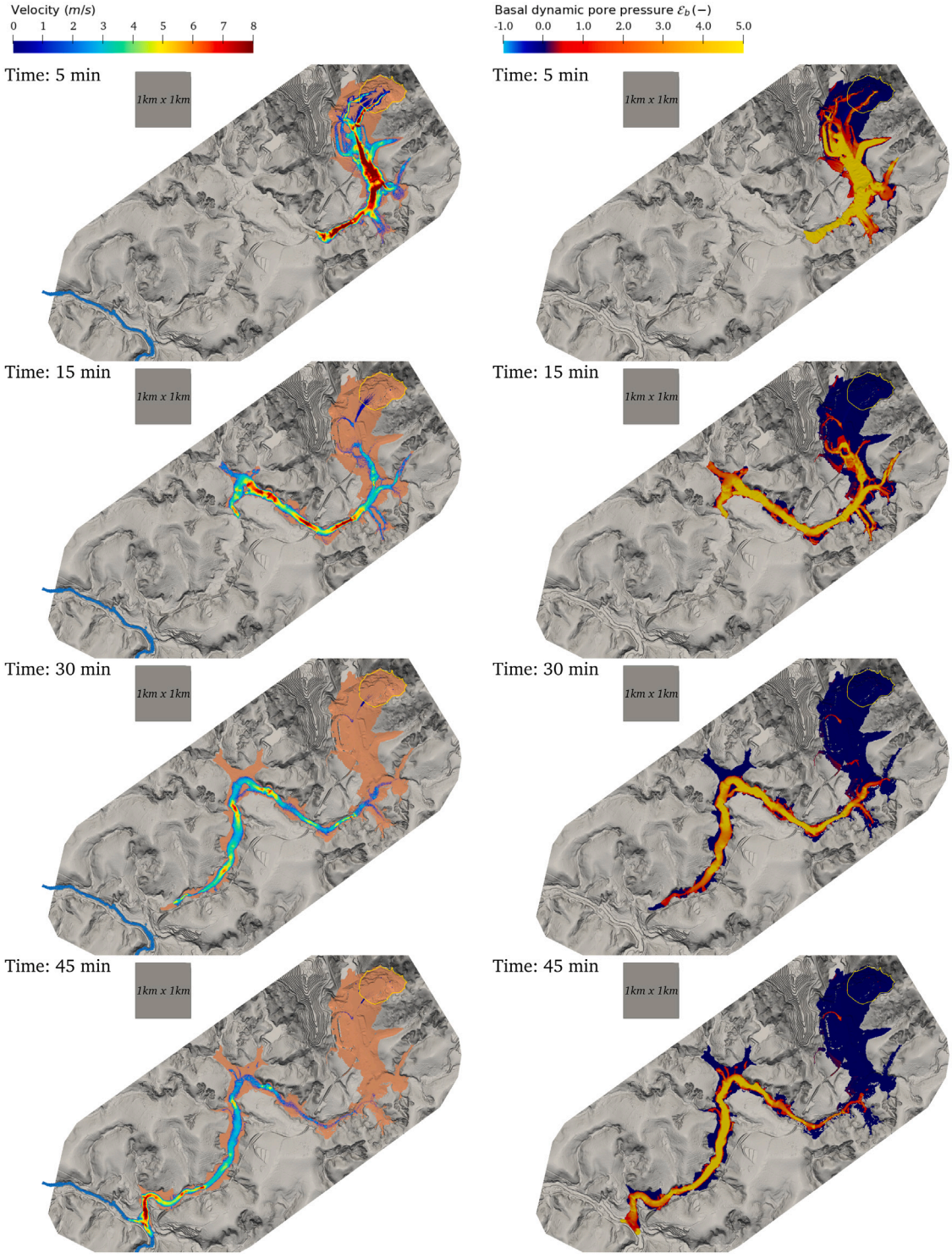

Fig. 21. Test C – Temporal evolution of (left) the flow velocity $\mathcal{U} = \sqrt{u^2 + v^2}$ and (right) the computed basal dynamic pore-pressure factor $\mathcal{E}_b$ at 5, 15, 30 and 45 minutes after the dam failure with pore-fluid viscosity $\mu = 0.002\,\mathrm{Pa}\cdot\mathrm{s}$.

solid flux at the edges which ensures the continuity equations of the system maintain their conservative character; second, it is possible to estimate a local value for the basal pore-pressure excess depending on the mixture packed state. Therefore, under the same flow conditions, dense packed mixtures are associated to a lower flow mobility whereas liquefied slurries are related to larger runout distances.

The proposed model is faced to a synthetic test, the widespread USGS debris dambreak experiments and the real-scale catastrophic mining tailings dam failure occurred in Brumadinho (Brazil,2019). In all these tests, the proposed approach reported physically-substantiated results, approaching the behaviour observed in this kind of flows. Especially, the model is able to replicate the separation of the solid aggregate from the pore-fluid phase during the movement and the persistence of high pressures within the pore-fluid. This sustains the flow mobility far way from the initialization zone and increases the runout distances. This novel mixing-layer model offers a promising starting-point for the development of robust, accurate and efficient

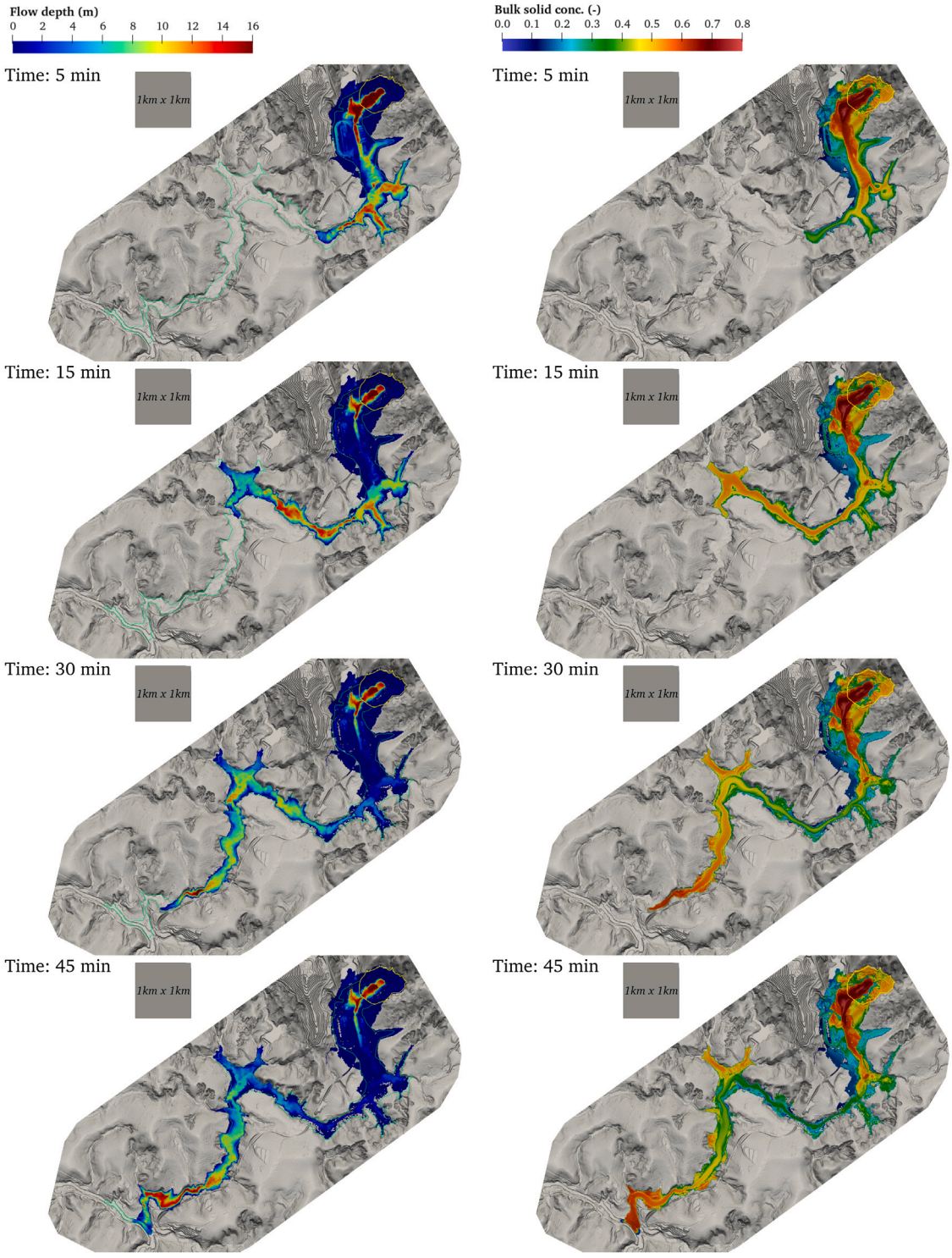

Fig. 22. Test C – Temporal evolution of (left) the computed flow depth h and (right) the bulk solid concentration ϕ at 5, 15, 30 and 45 minutes after the dam failure with pore-fluid viscosity $\mu = 0.002\,\mathrm{Pa}\cdot\mathrm{s}$.

simulation tools for these complex geophysical surface flows, able to be used in a predictive hazard system.

CRediT authorship contribution statement

S. Martínez-Aranda: Conceptualization, Investigation, Methodology, Software, Validation, Visualization, Writing – original draft, Writing – review & editing. **J. Fernández-Pato:** Methodology, Software. **P. García-Navarro:** Conceptualization, Funding acquisition, Project administration, Writing – review & editing.

Declaration of competing interest

The authors declare that they have no known competing financial interests or personal relationships that could have appeared to influence the work reported in this paper.

Data availability

Data will be made available on request.

Acknowledgements

This work was supported by grant PID2022-137334NB-I00 funded by MCIN/AEI/10.13039/501100011033 and by "ERDF/EU". Authors thank the U.S. Geological Survey (USGS) which supply the experimental data used in Section 5.2 and Hydronia LLC (www.hydronia.com) for providing information and advising in Section 5.3.

Appendix A. Depth-integration of the dilation drag term on the solid transport equation

In order to integrate the dilation drag term on the right hand side of Eq. (27) along the flow depth, boundary conditions for the specific discharge $\mathbf{q_w} = (q_{wx}, q_{wy}, q_{wz})$ must be imposed. At the fixed bed surface boundary $z_b = z_b(x, y)$, the solid grains and intergranular fluid move with the same velocity (non-penetration condition), leading to

$$(q_{wx})_b = (q_{wy})_b = (q_{wz})_b = 0 \tag{A.1}$$

whereas, at the flow free surface z_s, we assume the kinematic condition

$$(q_{wx})_s \frac{\partial z_s}{\partial x} + (q_{wy})_s \frac{\partial z_s}{\partial y} - (q_{wz})_s = 0 \tag{A.2}$$

implying a common free surface for both the solid and fluid phases which move with the flow free surface $z_s = z_s(t, x, y)$. Then, applying the Leibnitz integration rule, imposing (A.1)–(A.2) and considering the Darcy Law (11) to relate the specific discharge $\mathbf{q_w}$ to the dynamic pore pressure gradient ∇p_e, the depth-averaged source term on the right hand side term of (27) can be rewritten as

$$\begin{aligned}\int_{z_b}^{z_s} \nabla \cdot \left(\phi_p \frac{\rho_w}{\rho} \mathbf{q_w} \right) \mathrm{d}z = &- \frac{\partial}{\partial x} \int_{z_b}^{z_s} \left(\phi_p \frac{\rho_w}{\rho} \frac{\kappa}{\mu} \frac{\partial p_e}{\partial x} \right) \mathrm{d}z \\ &- \frac{\partial}{\partial y} \int_{z_b}^{z_s} \left(\phi_p \frac{\rho_w}{\rho} \frac{\kappa}{\mu} \frac{\partial p_e}{\partial y} \right) \mathrm{d}z\end{aligned} \tag{A.3}$$

Applying again the Leibnitz rule to each term on the right hand side of (A.3) and assuming the approximation $\phi_p/\rho = \overline{\phi}_p/\overline{\rho}$, for the sake of simplicity, leads to

$$\begin{aligned}&\int_{z_b}^{z_s} \left(\phi_p \frac{\rho_w}{\rho} \frac{\kappa}{\mu} \frac{\partial p_e}{\partial x} \right) \mathrm{d}z \\ &= \overline{\phi}_p \frac{\rho_w}{\overline{\rho}} \frac{\kappa}{\mu} \left(\frac{\partial}{\partial x} \int_{z_b}^{z_s} p_e \, \mathrm{d}z - (p_e)_s \frac{\partial z_s}{\partial x} + (p_e)_b \frac{\partial z_b}{\partial x} \right) = \overline{\phi}_p \frac{\rho_w}{\overline{\rho}} \mathcal{L}_x\end{aligned} \tag{A.4a}$$

$$\begin{aligned}&\int_{z_b}^{z_s} \left(\phi_p \frac{\rho_w}{\rho} \frac{\kappa}{\mu} \frac{\partial p_e}{\partial y} \right) \mathrm{d}z \\ &= \overline{\phi}_p \frac{\rho_w}{\overline{\rho}} \frac{\kappa}{\mu} \left(\frac{\partial}{\partial y} \int_{z_b}^{z_s} p_e \, \mathrm{d}z - (p_e)_s \frac{\partial z_s}{\partial y} + (p_e)_b \frac{\partial z_b}{\partial y} \right) = \overline{\phi}_p \frac{\rho_w}{\overline{\rho}} \mathcal{L}_y\end{aligned} \tag{A.4b}$$

where we have defined the deviatoric dilation fluxes along the x- and y-coordinates, $\mathcal{L}_x$ and $\mathcal{L}_y$ respectively, as

$$\begin{aligned}\mathcal{L}_x &= \frac{\kappa}{\mu} \left(\frac{\partial \mathcal{P}_e}{\partial x} + \mathcal{E}_b \rho_w g h \frac{\partial z_b}{\partial x} \right) \\ \mathcal{L}_y &= \frac{\kappa}{\mu} \left(\frac{\partial \mathcal{P}_e}{\partial y} + \mathcal{E}_b \rho_w g h \frac{\partial z_b}{\partial y} \right)\end{aligned} \tag{A.5}$$

being $\mathcal{P}_e$ the integral of the dynamic pore pressure along the flow column, written as

$$\mathcal{P}_e \equiv \int_{z_b}^{z_s} p_e \, \mathrm{d}z = \frac{-\mu h^3}{3\kappa} \dot{\gamma} \tan\psi \tag{A.6}$$

and $\mathcal{E}_b \rho_w g h$ the value of the dynamic pore pressure at the underlying bed surface, with $\mathcal{E}_b$ the basal dynamic pore pressure parameter defined in (16).

Note that using (A.4) allows to transform the non-conservative dilation source term (A.3) for the pth sediment class into a conservative deviatoric contribution $(\overline{\phi}_p \rho_w/\overline{\rho}\, \mathcal{L}_x,\ \overline{\phi}_p \rho_w/\overline{\rho}\, \mathcal{L}_y)$ to the convective solid flux depending on the pore-fluid pressure gradient. Hence, the depth-averaged solid phase transport equation for the pth sediment class (27) finally reads

$$\frac{\partial (h\overline{\phi}_p)}{\partial t} + \frac{\partial}{\partial x} \left(h\overline{u}\overline{\phi}_p + \mathcal{L}_x \frac{\rho_w}{\overline{\rho}} \overline{\phi}_p \right) + \frac{\partial}{\partial y} \left(h\overline{v}\overline{\phi}_p + \mathcal{L}_y \frac{\rho_w}{\overline{\rho}} \overline{\phi}_p \right) = 0 \tag{A.7}$$

Appendix B. Finite volume method derivation for density-variable shallow flows with solid dilation terms

To integrate the system (36) across the computational mesh, at each cell edge the local coordinates are defined following the normal $\mathbf{n}_k = (n_x, n_y)_k$ and tangential $\mathbf{t}_k = (-n_y, n_x)_k$ unit vectors to the cell edge. On the left hand side of (36), also called homogeneous part, the conservative flux matrix $\mathbf{E}(\mathbf{U})$ satisfies the rotation invariant property (Godlewski and Raviart, 1996; Toro, 1997) and hence

$$(\mathbf{E} \cdot \mathbf{n})_k = \left[\mathbf{F}(\mathbf{U}) n_x + \mathbf{G}(\mathbf{U}) n_y \right]_k = \mathbf{R}_k^{-1} \mathbf{F}(\mathbf{R}_k \mathbf{U}) \tag{B.1}$$

where the 4×4 rotation matrix $\mathbf{R}_k$ for the kth cell edge, and its inverse matrix $\mathbf{R}_k^{-1}$, are defined as

$$\mathbf{R}_k = \begin{pmatrix} 1 & 0 & 0 & 0 \\ 0 & n_x & n_y & 0 \\ 0 & -n_y & n_x & 0 \\ 0 & 0 & 0 & 1 \end{pmatrix}_k \qquad \mathbf{R}_k^{-1} = \begin{pmatrix} 1 & 0 & 0 & 0 \\ 0 & n_x & -n_y & 0 \\ 0 & n_y & n_x & 0 \\ 0 & 0 & 0 & 1 \end{pmatrix}_k \tag{B.2}$$

and $\mathbf{R}_k^{-1}$ denotes the inverse of the rotation matrix at the kth cell edge. The set of local conservative variables $\hat{\mathbf{U}} \equiv \mathbf{R}_k \mathbf{U}$ and the local homogeneous flux vector $\mathbf{F}(\hat{\mathbf{U}})_k \equiv \mathbf{F}(\mathbf{R}_k \mathbf{U})$ at the cell edge are defined as

$$\hat{\mathbf{U}} \equiv \mathbf{R}_k \mathbf{U} = \begin{pmatrix} rh \\ rhu_n \\ rhv_t \\ h\chi \end{pmatrix} \qquad \mathbf{F}(\hat{\mathbf{U}})_k \equiv \mathbf{F}(\mathbf{R}_k \mathbf{U}) = \begin{pmatrix} rhu_n \\ rhu_n^2 + \frac{1}{2} grh^2 \\ rhu_n v_t \\ hu_n \chi \end{pmatrix}_k \tag{B.3}$$

where $u_n = \mathbf{u} \cdot \mathbf{n} = un_x + vn_y$ and $v_t = \mathbf{u} \cdot \mathbf{t} = -un_y + vn_x$ are the flow velocity components in the local edge-framework, referred to as normal and shear velocity respectively.

In order to ensure a well-balanced formulation in steady flow states, the homogeneous flux through the kth cell edge $\mathbf{F}(\hat{\mathbf{U}})_k$ can be augmented with the non-conservative contribution of both the bed-pressure term $\mathbf{S_b}$ and the basal resistance term $\mathbf{S}_\tau$ (Castro et al., 2009; Murillo and Navas-Montilla, 2016), discretized as

$$\int_{\Omega_i} \mathbf{S_b}(\mathbf{U}) \, \mathrm{d}\Omega = \sum_{k=1}^{\mathrm{NE}} \mathbf{R}_k^{-1} \mathbf{H}(\hat{\mathbf{U}})_k \, l_k \tag{B.4a}$$

$$\int_{\Omega_i} \mathbf{S}_\tau(\mathbf{U}) \, \mathrm{d}\Omega = \sum_{k=1}^{\mathrm{NE}} \mathbf{R}_k^{-1} \mathbf{T}(\hat{\mathbf{U}})_k \, l_k \tag{B.4b}$$

where $\mathbf{H}(\hat{\mathbf{U}})_k$ is the integrated bed pressure through the edge (Murillo and García-Navarro, 2010) and $\mathbf{T}(\hat{\mathbf{U}})_k$ is the split contribution of the integrated basal resistance to the momentum at the kth cell edge (Martínez-Aranda et al., 2022), computed as

$$\mathbf{H}(\hat{\mathbf{U}})_k = \begin{pmatrix} 0 \\ -grh \, \Delta z_b \\ 0 \\ 0 \end{pmatrix}_k \qquad \mathbf{T}(\hat{\mathbf{U}})_k = \begin{pmatrix} 0 \\ -\frac{\tau_b}{\rho_w} (\Delta x \, n_{ux} + \Delta y \, n_{uy}) \\ 0 \\ 0 \end{pmatrix}_k \tag{B.5}$$

being $(\Delta x, \Delta y)$ the discrete horizontal distance and Δz_b the discrete bed level difference between the i–j cell centres.

Using (B.1), (B.4a) and (B.4b), the integral Eq. (36) is expressed as

$$\frac{\mathrm{d}}{\mathrm{d}t}\int_{\Omega_i}\mathbf{U}\,\mathrm{d}\Omega+\sum_{k=1}^{\mathrm{NE}}\mathbf{R}_k^{-1}\,\mathbf{F}(\hat{\mathbf{U}})_k\,l_k=\sum_{k=1}^{\mathrm{NE}}\mathbf{R}_k^{-1}\left(\mathbf{H}(\hat{\mathbf{U}})+\mathbf{T}(\hat{\mathbf{U}})\right)_k l_k - \sum_{k=1}^{\mathrm{NE}}(\mathbf{E}\cdot\mathbf{n})_k\,l_k \tag{B.6}$$

allowing to define the augmented numerical flux $\boldsymbol{F}(\hat{\mathbf{U}})_k$ for the kth cell edge as

$$\boldsymbol{F}(\hat{\mathbf{U}})_k=\left[\mathbf{F}(\hat{\mathbf{U}})-\mathbf{H}(\hat{\mathbf{U}})-\mathbf{T}(\hat{\mathbf{U}})\right]_k \tag{B.7}$$

Furthermore, the term in (B.6) related to the solid-phase dilation $\mathbf{L}(\mathbf{U})$ (34) satisfies the rotation invariant property and hence this deviatoric flux contribution can be expressed as

$$(\mathbf{E}\cdot\mathbf{n})_k=\left[\mathbf{L}_{\mathbf{x}}(\mathbf{U})\,n_x+\mathbf{L}_{\mathbf{y}}(\mathbf{U})\,n_y\right]_k=\mathbf{R}_k^{-1}\,\mathbf{L}_{\mathbf{n}}(\hat{\mathbf{U}})_k \tag{B.8}$$

with

$$\mathbf{L}_{\mathbf{n}}(\hat{\mathbf{U}})_k=\begin{pmatrix}0\\0\\0\\\mathcal{L}_n\,\dfrac{\chi}{r}\end{pmatrix}_k \tag{B.9}$$

being $\mathcal{L}_{nk}$ the dilation-induced deviatoric flux throughout the kth cell edge, expressed as

$$\mathcal{L}_{nk}=\left[\frac{\kappa}{\mu}\left(\frac{\partial\mathcal{P}_e}{\partial\hat{n}}+\mathcal{E}_b\rho_w g h\frac{\partial z_b}{\partial\hat{n}}\right)\right]_k \tag{B.10}$$

where $\hat{n}$ is the local unit normal vector to the cell edge. Using the augmented flux (B.7) and the deviatoric dilation flux (B.9), the integral Eq. (B.6) can be finally rewritten as

$$\frac{\mathrm{d}}{\mathrm{d}t}\int_{\Omega_i}\mathbf{U}\,\mathrm{d}\Omega=-\sum_{k=1}^{\mathrm{NE}}\mathbf{R}_k^{-1}\left(\boldsymbol{F}(\hat{\mathbf{U}})+\mathbf{L}_{\mathbf{n}}(\hat{\mathbf{U}})\right)_k l_k \tag{B.11}$$

Assuming piecewise uniform conservative variables $\mathbf{U}$ for the i cell at each time $t=t^n$ and using first-order explicit temporal integration, the value of the conservative variables $\mathbf{U}$ at the cells can be updated as

$$\mathbf{U}_i^{n+1}=\mathbf{U}_i^n-\frac{\Delta t}{A_i}\sum_{k=1}^{\mathrm{NE}}\mathbf{R}_k^{-1}\,\boldsymbol{\mathcal{F}}_k^{\downarrow}\,l_k \tag{B.12}$$

being A_i the discrete cell area, $\Delta t=t^{n+1}-t^n$ the time step and $\boldsymbol{\mathcal{F}}_k^{\downarrow}=\boldsymbol{F}_k^{\downarrow-}+\mathbf{L}_{\mathbf{n}k}^{\downarrow-}$ the explicit (upwind) flux throughout the kth cell edge, including the augmented flux (conservative fluxes plus bed-pressure contribution plus basal resistance split term) supplemented by the deviatoric dilation-related contribution to the solid flux.

Appendix C. Augmented upwind flux computation

In this work, this augmented flux vector is computed using the approximate Riemann problem (RP) theory and a first-order Roe's solver for density-variable shallow flows. Details on the flux computation have been extensively reported in Martínez-Aranda et al. (2020), Martínez-Aranda (2021) and Martínez-Aranda et al. (2021) but, for the sake of completeness, a summary is included here. The augmented flux vector $\boldsymbol{F}_k$ at the kth edge between the left cell i and the right cell j, including the conservative fluxes and the non-conservative bed-pressure and basal resistance momentum terms, is expressed as

$$\boldsymbol{F}_k=\mathbf{F}(\hat{\mathbf{U}}_i^n,\hat{\mathbf{U}}_j^n)_k-\mathbf{H}(\hat{\mathbf{U}}_i^n,\hat{\mathbf{U}}_j^n)_k-\mathbf{T}(\hat{\mathbf{U}}_i^n,\hat{\mathbf{U}}_j^n)_k \tag{C.1}$$

and its computation is based on the conservative Jacobian $\widetilde{\mathbf{J}}_k(\hat{\mathbf{U}}_i^n,\hat{\mathbf{U}}_j^n)$, defined as

$$\widetilde{\mathbf{J}}_k=\left(\frac{\partial\mathbf{F}(\hat{\mathbf{U}})}{\partial\hat{\mathbf{U}}}\right)_k=\begin{pmatrix}0 & 1 & 0 & 0\\ \frac{1}{2}g\widetilde{h}(1+\widetilde{r})-\widetilde{u}_n^2 & 2\widetilde{u}_n & 0 & -\frac{1}{2}g\widetilde{h}\widetilde{r}\\ -\widetilde{u}_n\,\widetilde{v}_t & \widetilde{v}_t & \widetilde{u}_n & 0\\ -\widetilde{u}_n\,\widetilde{\chi}/\widetilde{r} & \widetilde{\chi}/\widetilde{r} & 0 & \widetilde{u}_n\end{pmatrix}_k \tag{C.2}$$

where the $\widetilde{h}$ is the edge-averaged flow depth, $\widetilde{r}$ is the edge-averaged bulk density, $\widetilde{\chi}$ is the edge-averaged buoyant solid concentration and $(\widetilde{u}_n,\widetilde{v}_t)$ are the edge-averaged normal and tangential velocity, respectively, to the kth cell edge.

The approximate matrix $\widetilde{\mathbf{J}}_k$ (C.2) has four different real eigenvalues

$$\widetilde{\lambda}_{1,k}=(\widetilde{u}_n-\widetilde{c})_k\qquad\widetilde{\lambda}_{2,k}=(\widetilde{u}_n)_k\qquad\widetilde{\lambda}_{3,k}=(\widetilde{u}_n+\widetilde{c})_k\qquad\widetilde{\lambda}_{4,k}=(\widetilde{u}_n)_k \tag{C.3}$$

being $\widetilde{c}_k$ the edge-averaged celerity, defined as

$$\widetilde{c}_k=\left(\sqrt{\frac{1}{2}g\widetilde{h}\,\left(1+\widetilde{r}-\widetilde{\chi}\right)}\right)_k \tag{C.4}$$

and allowing to diagonalize the matrix as $\widetilde{\mathbf{J}}_k=(\widetilde{\mathbf{P}}\widetilde{\boldsymbol{\Lambda}}\widetilde{\mathbf{P}}^{-1})_k$, where $\widetilde{\boldsymbol{\Lambda}}_k$ is a diagonal matrix containing the eigenvalues $\lambda_{m,k}$, the matrix $\widetilde{\mathbf{P}}_k=(\widetilde{\mathbf{e}}_1,\widetilde{\mathbf{e}}_2,\widetilde{\mathbf{e}}_3,\widetilde{\mathbf{e}}_4)_k$ contains the orthogonal basis of eigenvectors $(\widetilde{\mathbf{e}}_m)_k$ and $\widetilde{\mathbf{P}}_k^{-1}$ denotes its inverse matrix.

According the Roe linearization, the numerical frictionless flux at the kth cell edge $\boldsymbol{F}_k^{\downarrow}$ is provided by a discontinuous flux function constructed by defining appropriate Rankine–Hugoniot (RH) relations across each moving wave $\lambda_{m,k}$. The upwind value of the frictionless flux vector for the i cell can be computed as

$$\boldsymbol{F}_k^{\downarrow-}=\mathbf{F}(\hat{\mathbf{U}}_i^n)+\sum_{m-}\left[(\widetilde{\lambda}_m\widetilde{\alpha}_m-\widetilde{\beta}_m-\widetilde{\sigma}_m)\widetilde{\mathbf{e}}_m\right]_k^n \tag{C.5}$$

where the subscript $m-$ under the sums indicate waves travelling inward the i cell. The coefficients $\widetilde{\alpha}_{m,k}$ denote the wave strengths accounting for the discontinuity on the conservative variables between cell centre, $\hat{\mathbf{U}}_j^n-\hat{\mathbf{U}}_i^n$, the coefficients $\widetilde{\beta}_{m,k}$ are the source strengths which include the integrated bed pressure through the cell edge, $\mathbf{H}(\hat{\mathbf{U}}_i^n,\hat{\mathbf{U}}_j^n)_k$, and the coefficients $\widetilde{\sigma}_{m,k}$ are the source strengths accounting for the split basal resistance contribution at the cell edge, $\mathbf{T}(\hat{\mathbf{U}}_i^n,\hat{\mathbf{U}}_j^n)_k$, all of them satisfying

$$\hat{\mathbf{U}}_j^n-\hat{\mathbf{U}}_i^n=\sum_{m=1}^{4}(\widetilde{\alpha}_m\widetilde{\mathbf{e}}_m)_k^n \tag{C.6a}$$

$$\mathbf{H}(\hat{\mathbf{U}}_i^n,\hat{\mathbf{U}}_j^n)_k=\sum_{m=1}^{4}(\widetilde{\beta}_m\widetilde{\mathbf{e}}_m)_k^n \tag{C.6b}$$

$$\mathbf{T}(\hat{\mathbf{U}}_i^n,\hat{\mathbf{U}}_j^n)_k=\sum_{m=1}^{4}(\widetilde{\sigma}_m\widetilde{\mathbf{e}}_m)_k^n \tag{C.6c}$$

The deviatoric solid dilation contribution to the intercell flux throughout the kth edge can be expressed as

$$\mathbf{L}_{\mathbf{n}k}=\mathbf{L}_{\mathbf{n}}(\hat{\mathbf{U}}_i^n,\hat{\mathbf{U}}_j^n)_k \tag{C.7}$$

and it is computed using a first-order upwind approximation as

$$\mathbf{L}_{\mathbf{n}k}^{\downarrow-}=\begin{pmatrix}0\\0\\0\\\widetilde{\mathcal{L}}_{nk}\left(\dfrac{\chi}{r}\right)_{\{upw\}}\end{pmatrix}\quad\text{with}:\begin{cases}\{upw\}=i & \text{if}\quad \boldsymbol{\mathcal{F}}_k^{\{1\}\downarrow}\geq 0\\ \{upw\}=j & \text{if}\quad \boldsymbol{\mathcal{F}}_k^{\{1\}\downarrow}<0\end{cases} \tag{C.8}$$

where $\widetilde{\mathcal{L}}_{nk}$ is the edge-averaged value of the deviatoric dilation-relation contribution at the kth cell edge, computed as

$$\widetilde{\mathcal{L}}_{nk}=\left[\frac{\widetilde{\kappa}}{\widetilde{\mu}}\left(\frac{\Delta\mathcal{P}_e}{d_n}+\widetilde{\mathcal{E}}_b\rho_w g\widetilde{h}\frac{\Delta z_b}{d_n}\right)\right]_k \tag{C.9}$$

being d_n the normal-distance between cell centres.

Finally, the stability of the explicitly computed numerical solution is ensured by imposing that the time step is small enough to avoid the interaction of waves from neighbouring Riemann problems. The maximum local time step allowed at the kth edge, Δt_k, is estimate here

by assuming that the fastest wave celerity corresponds to the absolute maximum of the eigenvalues of the Jacobian $\widetilde{\mathbf{J}}_k$ (C.2) as

$$\Delta t_k = \frac{\min(A_i, A_j)}{l_k \max\left(|\widetilde{\lambda}_{1,k}|, |\widetilde{\lambda}_{3,k}|\right)} \tag{C.10}$$

and the global time step $\Delta t = t^{n+1} - t^n$ is limited using the minimum of the local time steps and the Courant–Friedrichs–Lewy (CFL) condition

$$\mathrm{CFL} = \frac{\Delta t}{\min_k(\Delta t_k)} \tag{C.11}$$

with CFL < 0.5 for square-orthogonal grids and CFL < 1 for both triangular topology and 1D-mesh cases.

References

Armanini, A., Fraccarollo, L., Rosatti, G., 2009. Two-dimensional simulation of debris flows in erodible channels. Comput. Geosci. 35, 993–1006.

Baumgarten, A.S., Kamrin, K., 2019. A general fluid–sediment mixture model and constitutive theory validated in many flow regimes. J. Fluid Mech. 861, 721–764.

Berti, M., Genevois, R., Simoni, A., Tecca, P.R., 1999. Field observations of a debris flow event in the Dolomites. Geomorphology 29, 265–274.

Berti, M., Simoni, A., 2005. Experimental evidences and numerical modeling of debris flow initiated by channel runoff. Landslides.

Bouchut, F., Fernández-Nieto, E.D., Mangeney, A., Narbona-Reina, G., 2016. A two-phase two-layer model for fluidized granular flows with dilatancy effects. J. Fluid Mech. 801, 166–221.

Brufau, P., Garcia-Navarro, P., Ghilardi, P., Natale, L., Savi, F., 2000. 1D mathematical modelling of debris flow. J. Hydraul. Res. 38, 435–446.

Calhoun, N.C., Clague, J.J., 2018. Distinguishing between debris flows and hyperconcentrated flows: An example from the eastern Swiss Alps. Earth Surf. Process. Landf. 43, 1280–1294.

Castro, M., Fernández-Nieto, E., Ferreiro, A., García-Rodríguez, J., Parés, C., 2009. High order extensions of roe schemes for two-dimensional nonconservative hyperbolic systems. J. Sci. Comput. 39, 67–114.

Castro-Orgaz, O., Hager, W.H., 2017. Non-Hydrostatic Free Surface Flows. Springer, Cham.

Cui, K.F.E., Zhou, G.G.D., Jing, L., 2021. Viscous effects on the particle size segregation in geophysical mass flows: Insights from immersed granular shear flow simulations. J. Geophys. Res. Solid Earth 126, e2021JB022274.

Cui, K.F.E., Zhou, G.G.D., Jing, L., 2022. Particle segregation and diffusion in fluid-saturated granular shear flows. Phys. Rev. Fluids 7, 014305.

Cui, K.F.E., Zhou, G.G.D., Jing, L., Chen, X., Song, D., 2020. Generalized friction and dilatancy laws for immersed granular flows consisting of large and small particles. Phys. Fluids 32, 113312.

Denlinger, R.P., Iverson, R.M., 2001. Flow of variably fluidized granular masses across three-dimensional terrain: 2. Numerical predictions and experimental tests. J. Geophys. Res. Solid Earth 106, 553–566.

Dewals, B., Rulot, F., Erpicum, S., Archambeau, P., Pirotton, M., 2011. Sediment Transport. IntechOpen.

Ding, W.-T., Xu, W.-J., 2018. Study on the multiphase fluid-solid interaction in granular materials based on an LBM-DEM coupled method. Powder Technol. 335, 301–314.

Fleming, R.W., Ellen, S.D., Algus, M.A., 1989. Transformation of dilative and contractive landslide debris into debris flows—An example from marin County, California. Eng. Geol. 27, 201–223.

Forterre, Y., Pouliquen, O., 2008. Flows of dense granular media. Annu. Rev. Fluid Mech. 40, 1–24.

Fraccarollo, L., Capart, H., Zech, Y., 2003. A Godunov method for the computation of erosional shallow water transients. Internat. J. Numer. Methods Fluids 41, 951–976.

George, L., Iverson, M., 2011. A two-phase debris-flow model that includes coupled evolution of volume fractions, granular dilatancy and pore-fluid pressure. In: 5th International Conference on Debris-Flow Hazards: Mitigation, Mechanics, Prediction and Assessment. p. 10.

George, D.L., Iverson, R.M., 2014. A depth-averaged debris-flow model that includes the effects of evolving dilatancy. II. Numerical predictions and experimental tests. Proc. R. Soc. Lond. Ser. A Math. Phys. Eng. Sci. 470, 20130820.

Godlewski, E., Raviart, P.-A., 1996. Numerical Approximation of Hyperbolic Systems of Conservation Laws. Springer-Verlag, New York.

Greco, M., Di Cristo, C., Iervolino, M., Vacca, A., 2019. Numerical simulation of mud-flows impacting structures. J. Mt. Sci. 16, 364–382.

Haitjema, H.M., Anderson, M.P., 2016. Darcy velocity is not a velocity. Groundwater 54, 1.

Hess, J., Tai, Y.-C., Wang, Y., 2019. Debris flows with pore pressure and intergranular friction on rugged topography. Comput. & Fluids 190, 139–155.

Heyman, J., Delannay, R., Tabuteau, H., Valance, A., 2017. Compressibility regularizes the $\mu(I)$-rheology for dense granular flows. J. Fluid Mech. 830, 553–568.

Hungr, O., Evans, S.G., Bovis, M.J., Hutchinson, J.N., 2001. A review of the classification of landslides of the flow type. Environ. Eng. Geosci. 7, 221–238.

Hungr, O., McDougall, S., 2009. Two numerical models for landslide dynamic analysis. Comput. Geosci. 35, 978–992.

Iverson, R.M., 1997. The physics of debris flows. Rev. Geophys. 35, 245–296.

Iverson, R.M., Denlinger, R.P., 2001. Flow of variably fluidized granular masses across three-dimensional terrain: 1. Coulomb mixture theory. J. Geophys. Res. Solid Earth 106, 537–552.

Iverson, R.M., George, D.L., 2014. A depth-averaged debris-flow model that includes the effects of evolving dilatancy. I. Physical basis. Proc. R. Soc. Lond. Ser. A Math. Phys. Eng. Sci. 470, 20130819.

Iverson, R.M., Logan, M., LaHusen, R.G., Berti, M., 2010. The perfect debris flow? Aggregated results from 28 large-scale experiments. J. Geophys. Res. Earth Surf. 115, F03005.

Iverson, R.M., Reid, M.E., Logan, M., LaHusen, R.G., Godt, J.W., Griswold, J.P., 2011. Positive feedback and momentum growth during debris-flow entrainment of wet bed sediment. Nat. Geosci. 4, 116–121.

Iverson, R.M., Vallance, J.W., 2001. New views of granular mass flows. Geology 29, 115–118.

Jakob, M., Hungr, O., 2005. Debris-flow Hazards and Related Phenomena. In: Springer Praxis Books, Springer Berlin Heidelberg.

Juez, C., Caviedes-Voullieme, D., Murillo, J., García-Navarro, P., 2014. 2D dry granular free-surface transient flow over complex topography with obstacles. Part II: Numerical predictions of fluid structures and benchmarking. Comput. Geosci. 73, 142–163.

Kowalski, J., 2008. Two-Phase Modeling of Debris Flows (Ph.D. thesis). ETH Zurich, Switzerland.

Kowalski, J., McElwaine, J.N., 2013. Shallow two-component gravity-driven flows with vertical variation. J. Fluid Mech. 714, 434–462.

Lancaster, S.T., Hayes, S.K., Grant, G.E., 2003. Effects of wood on debris flow runout in small mountain watersheds. Water Resour. Res. 39, 21.

Lee, C.-H., 2021. Two-phase modelling of submarine granular flows with shear-induced volume change and pore-pressure feedback. J. Fluid Mech. 907, A31.

Li, J., Cao, Z., Hu, K., Pender, G., Liu, Q., 2018. A depth-averaged two-phase model for debris flows over erodible beds. Earth Surf. Process. Landf. 43, 817–839.

Luna, B.Q., Remaître, A., van Asch, T., Malet, J.-P., van Westen, C., 2012. Analysis of debris flow behavior with a one dimensional run-out model incorporating entrainment. Eng. Geol. 128, 63–75.

Major, J.J., Iverson, R.M., 1999. Debris-flow deposition: Effects of pore-fluid pressure and friction concentrated at flow margins. GSA Bull. 111, 1424–1434.

Mari, R., Seto, R., Morris, J.F., Denn, M.M., 2014. Shear thickening, frictionless and frictional rheologies in non-Brownian suspensions. J. Rheol. 58, 1693–1724.

Martínez-Aranda, S., 2021. Efficient Simulation Tools (EST) for Sediment Transport in Geomorphological Shallow Flows (Ph.D. thesis). Universiy of Zaragoza, Spain.

Martínez-Aranda, S., Murillo, J., García-Navarro, P., 2020. A robust two-dimensional model for highly sediment-laden unsteady flows of variable density over movable beds. J. Hydroinform. 22, 1138–1160.

Martínez-Aranda, S., Murillo, J., García-Navarro, P., 2021. A GPU-accelerated efficient simulation tool (EST) for 2D variable-density mud/debris flows over non-uniform erodible beds. Eng. Geol. 296, 106462.

Martínez-Aranda, S., Murillo, J., Morales-Hernández, M., García-Navarro, P., 2022. Novel discretization strategies for the 2D non-Newtonian resistance term in geophysical shallow flows. Eng. Geol. 302, 106625.

McArdell, B.W., Bartelt, P., Kowalski, J., 2007. Field observations of basal forces and fluid pore pressure in a debris flow. Geophys. Res. Lett. 34, L07406.

Meng, X., Wang, Y., 2016. Modelling and numerical simulation of two-phase debris flows. Acta Geotech. 11, 1027–1045.

Meyrat, G., McArdell, B., Ivanova, K., Müller, C., Bartelt, P., 2022. A dilatant, two-layer debris flow model validated by flow density measurements at the swiss illgraben test site. Landslides 19, 265–276.

Montellà, E., Chauchat, J., Bonamy, C., Weij, D., Keetels, G., Hsu, T., 2023. Numerical investigation of mode failures in submerged granular columns. Flow 3, E28.

Montellà, E., Chauchat, J., Chareyre, B., Bonamy, C., Hsu, T., 2021. A two-fluid model for immersed granular avalanches with dilatancy effects. J. Fluid Mech. 925, A13.

Murillo, J., García-Navarro, P., 2010. Weak solutions for partial differential equations with source terms: Application to the shallow water equations. J. Comput. Phys. 229, 4327–4368.

Murillo, J., García-Navarro, P., 2012. Wave Riemann description of friction terms in unsteady shallow flows: Application to water and mud/debris floods. J. Comput. Phys. 231, 1963–2001.

Murillo, J., Navas-Montilla, A., 2016. A comprehensive explanation and exercise of the source terms in hyperbolic systems using roe type solutions. Application to the 1D-2D shallow water equations. Adv. Water Resour. 98, 70–96.

O'Brien, J.S., Julien, P.Y., Fullerton, W.T., 1993. Two-dimensional water flood and mudflow simulation. J. Hydraul. Eng. 119, 244–261.

Ouyang, C., He, S., Tang, C., 2015a. Numerical analysis of dynamics of debris flow over erodible beds in wenchuan earthquake-induced area. Eng. Geol. 194, 62–72.

Ouyang, C., He, S., Xu, Q., 2015b. MacCormack-TVD finite difference solution for dam break hydraulics over erodible sediment beds. J. Hydraul. Eng. 141, 06014026.

Pailha, M., Pouliquen, O., 2009. A two-phase flow description of the initiation of underwater granular avalanches. J. Fluid Mech. 633, 115–135.

Pastor, M., Blanc, T., Haddad, B., Drempetic, V., Sanchez-Morles, M., Dutto, P., Martin-Stickle, M., Mira, P., Fernández-Merodo, J., 2015. Depth averaged models for fast landslide propagation: Mathematical, rheological and numerical aspects. Arch. Comput. Methods Eng. 22, 67–104.

Pelanti, M., Bouchut, F., Mangeney, A., 2008. A roe-type scheme for two-phase shallow granular flows over variable topography. ESAIM Math. Model. Numer. Anal. 42, 851–885.

Pierson, T., 2005. Hyperconcentrated Flow – Transitional Process Between Water Flow and Debris Flow. Debris-flow Hazards and Related Phenomena. Springer Berlin Heidelberg, Berlin, Germany.

Pitman, E.B., Le, L., 2005. A two-fluid model for avalanche and debris flows. Phil. Trans. R. Soc. A 363, 1573–1601.

Quecedo, M., Pastor, M., Herreros, M.I., Fernández Merodo, J.A., 2004. Numerical modelling of the propagation of fast landslides using the finite element method. Internat. J. Numer. Methods Engrg. 59, 755–794.

Robertson, P., de Melo, L., Williams, D., Wilson, G.W., 2019. Report of the Expert Panel on the Technical Causes of the Failure of Feijão Dam I. Technical Report, Vale S.A..

Rodine, J., Johnson, A., 1976. The ability of debris, heavily freighted with coarse clastic materials, to flow on gentle slopes. Sedimentology 23, 213–234.

Sassa, K., 1984. The mechanism starting liquefied landslides and debris flows. In: IV Int. Symp. Landslides, vol. 2, Toronto, pp. 349–354.

Toro, E., 1997. Riemann Solvers and Numerical Methods for Fluid Dynamics: A Practical Introduction. Springer-Verlag, Berlin, Germany.

Tsigginos, C., Meng, J., Gu, X.-J., Emerson, D.R., 2022. Coupled LBM-DEM simulations using the partially saturated method: Theoretical and computational aspects. Powder Technol. 405, 117556.

Vicari, H., Tran, Q.A., Nordal, S., Thakur, V., 2022. MPM modelling of debris flow entrainment and interaction with an upstream flexible barrier. Landslides 19, 2101–2115.

Whitaker, S., 1986. Flow in porous media I: A theoretical derivation of Darcy's law. Transp. Porous Media 1, 3–25.

Wu, W., 2007. Computational River Dynamics. NetLibrary, Inc, CRC Press.

Xia, C., Li, J., Cao, Z., Liu, Q., Hu, K., 2018. A quasi single-phase model for debris flows and its comparison with a two-phase model. J. Mt. Sci. 15, 1071–1089.

Zhou, G.G.D., Cui, K.F.E., Jing, L., Zhao, T., Song, D., Huang, Y., 2020. Particle size segregation in granular mass flows with different ambient fluids. J. Geophys. Res. Solid Earth 125, e2020JB019536.